



1 Development of the DRoplet Ice Nuclei Counter Zürich (DRINCZ): 2 Validation and application to field collected snow samples

3 Robert O. David^{1,*}, Maria Cascajo Castresana^{1,2}, Killian P. Brennan¹, Michael Rösch¹, Nora Els⁴, Julia
4 Werz³, Vera Weichlinger¹, Lin S. Boynton³, Sophie Bogler³, Nadine Borduas-Dedekind^{1,3}, Claudia
5 Marcolli¹, Zamin A. Kanji¹

6 ¹Institute of Atmospheric and Climate Science, ETH Zürich, Zürich, 8092, Switzerland

7 ²CIC nanoGUNE Consolider, Donostia-San Sebastian, E-20018, Spain

8 ³Institute for Biogeochemistry and Pollutant Dynamics, ETH Zürich, Zürich, 8092, Switzerland

9 ⁴Institute of Ecology, University of Innsbruck, Innsbruck, 6020, Austria

10 *Now at Department of Geosciences, University of Oslo, Oslo, 0315, Norway

11

12 *Correspondence to:* Robert O. David (r.o.david@geo.uio.no) and Zamin A. Kanji (zamin.kanji@env.ethz.ch)

13 **Abstract.** Ice formation in the atmosphere is important for regulating cloud lifetime, Earth's radiative balance and initiating
14 precipitation. Due to the difference in the saturation vapor pressure over ice and water, in mixed-phase clouds (MPCs), ice
15 will grow at the expense of supercooled cloud droplets. As such, MPCs, which contain both supercooled liquid and ice, are
16 particularly susceptible to ice formation. However, measuring and quantifying the concentration of ice nucleating particles
17 (INPs) responsible for ice formation at temperatures associated with MPCs is challenging due to their very low concentrations
18 in the atmosphere (~ 1 in 10^5 at -30 °C). Atmospheric INP concentrations vary over several orders of magnitude at a single
19 temperature and strongly increase as temperature approaches the homogeneous freezing threshold of water. To further quantify
20 the INP concentration in nature and perform systematic laboratory studies to increase the understanding of the properties
21 responsible for ice nucleation, a new drop freezing instrument, the DRoplet Ice Nuclei Counter Zurich (DRINCZ) is developed.
22 The instrument is based on the design of previous drop freezing assays and uses a USB camera to automatically detect freezing
23 in a 96-well tray cooled in an ethanol chilled bath with an automated analysis procedure. Based on an in-depth characterization
24 of DRINCZ, we develop a new method for quantifying and correcting temperature biases across drop freezing assays. DRINCZ
25 is further validated performing NX-illite experiments, which compare well with the literature. The temperature uncertainty in
26 DRINCZ was determined to be ± 0.9 °C. Furthermore, we demonstrate the applicability of DRINCZ by measuring and
27 analyzing field collected snow samples during an evolving synoptic situation in the Austrian Alps. The field samples fall within
28 previously observed ranges for cumulative INP concentrations and show a dependence on air mass origin and upstream
29 precipitation amount.



30 **1 Introduction**

31 In the atmosphere, ice plays an important role in initiating precipitation and affects the radiative properties of clouds. As much
32 as 80% of land falling precipitation initiates through the ice phase (Mülmenstädt et al., 2015), making it essential to understand
33 the pathways for ice formation in the atmosphere. The ratio of cloud droplets to ice crystals in a mixed-phase cloud (MPC)
34 alters the radiative properties of the cloud and its lifetime (Lohmann and Feichter, 2005; Matus and L'Ecuyer, 2017; Tan et
35 al., 2016). This ratio is important for future climate projections as warmer temperatures will lead to a decrease in ice content,
36 ultimately increasing cloud lifetime and cloud albedo (Tan et al., 2016). Additionally, ice formation at temperatures above
37 $-38\text{ }^{\circ}\text{C}$ in the atmosphere occurs primarily in MPCs through the freezing of cloud droplets (Ansmann et al., 2009; Boer et al.,
38 2011; Westbrook and Illingworth, 2011). Therefore, understanding ice formation in conditions associated with MPCs is of the
39 utmost importance.

40
41 When an ice nucleating particle (INP) gets immersed in cloud droplets either by acting as cloud condensation nucleus or
42 through scavenging by cloud droplets, the INP can induce ice formation by reducing the energy barrier associated with the
43 formation of an ice germ and thus freeze at warmer temperatures than homogeneous freezing (Vali et al., 2015). To reproduce
44 the immersion freezing pathway in the laboratory, several methods are used. Single particle methods, such as continuous flow
45 diffusion chambers (Rogers, 1988; Stetzer et al., 2008) operated at water supersaturated conditions (DeMott et al., 2015, 2017;
46 Hiranuma et al., 2015), or with extended chambers that activate individual particles into cloud droplets before exposing them
47 to supercooled conditions (Burkert-Kohn et al., 2017; Kohn et al., 2016; Lüönd et al., 2010) allow for the quantification of the
48 number concentration of INPs as a function temperature. Larger laboratory based single particle methods for examining INPs
49 in the immersion mode include expansion chambers where cloud droplets are first formed by adiabatic cooling due to the
50 expansion of an air volume (Niemand et al., 2012) or experiments where droplets are initially activated and then subsequently
51 cooled as they travel through a laminar flow tube (Hartmann et al., 2011). However, the single particle methods have detection
52 limitations due to the background ice crystal concentration of the chamber and the optical methods for discriminating between
53 ice and water. Due to the rarity of INPs at MPC conditions, single particle methods are typically unable to quantify INP
54 concentrations within natural ambient samples at temperatures higher than approximately $-22\text{ }^{\circ}\text{C}$ in remote regions or without
55 the use of concentrators (Cziczo et al., 2017).

56
57 In contrast bulk methods such as, drop freezing assays (Bigg, 1953; Hill et al., 2014; Stopelli et al., 2014; Vali, 1971),
58 differential scanning calorimetry (Kaufmann et al., 2017; Marcolli et al., 2007) and microfluidic devices (Reicher et al., 2018;
59 Riechers et al., 2013; Stan et al., 2009; Tarn et al., 2018) can be used to detect even the lowest atmospheric INP concentrations.
60 The majority of atmospheric INP concentrations at temperatures above $-15\text{ }^{\circ}\text{C}$ has been quantified using drop freezing assays.
61 To retrieve the concentrations of INP from such bulk suspensions, Vali, (1971; 2019) showed that by dividing a sample into
62 several aliquots, it is possible to calculate the number of INPs present in the sample as a function of temperature. The



63 probability for more than one INP in an aliquot that freezes at the same temperature can be predicted using Poisson's Law
64 (Vali, 1971). Following Vali (1971), the cumulative number of INPs in a given sample for each temperature can be calculated
65 as:

$$66 \quad INP(T) = \frac{-\ln(1-FF(T))}{V_a} \quad (1)$$

67 where $FF(T)$ is the fraction of frozen aliquots at a given temperature, T , and V_a is the volume of an aliquot. As can be seen in
68 Eq. 1, the only way to extend the range of measureable INPs across temperature scales is to change V_a . Due to instrumental
69 limitations, it is often difficult to change V_a by significantly enough values for a change in $INP(T)$ within a single instrumental
70 setup. Rather it is easier to dilute the initial sample thereby reducing the number of INPs in each aliquot. To account for
71 dilution, Eq. 1 can be rewritten as:

$$72 \quad INP(T) = \frac{-\ln(1-FF(T))DF}{V_a} \quad (2)$$

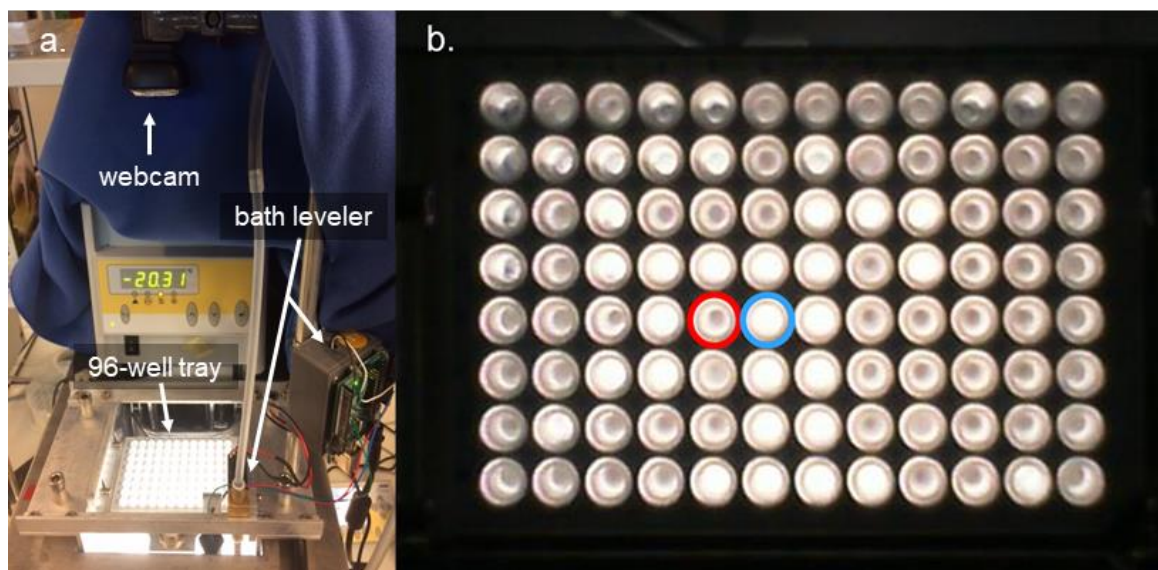
73 where DF is the dilution factor of the initial sample. However, in some cases dilution alone cannot be used to observe the total
74 number of $INP(T)$ due to the presence of impurities that act as INPs in the water used for dilution (Polen et al., 2018).
75 Therefore, it is necessary to use different bulk techniques that measure aliquots with volumes that span several orders of
76 magnitude, typically microliter to picoliter volumes (Harrison et al., 2018; Hill et al., 2014; Murray et al., 2010; Whale et al.,
77 2015).

78
79 Studies have investigated the concentrations of INPs in the atmosphere over the last 50 years and show that the concentration
80 in the atmosphere spans several orders of magnitude (Fletcher, 1962; Kanji et al., 2017; Petters and Wright, 2015; Welti et al.,
81 2018). Some of the original studies investigated the INP concentrations in melted hail and snow samples e.g. (Bigg, 1953;
82 Vali, 1971). Since then, studies have diversified to sampling INPs directly from the air (Boose et al., 2016b; Creamean et al.,
83 2013; DeMott et al., 2003; Lacher et al., 2017; Richardson et al., 2007; Welti et al., 2018), from precipitation (Christner et al.,
84 2008; Hill et al., 2014; Petters and Wright, 2015; Stopelli et al., 2015) and investigated potential types of INPs in the laboratory
85 from commercial and naturally occurring samples as well as field collected samples (Atkinson et al., 2013; Boose et al., 2016a;
86 Broadley et al., 2012; Felgitsch et al., 2018; Hill et al., 2014; Hiranuma et al., 2015, 2019; Kaufmann et al., 2016; Murray et
87 al., 2012; Pummer et al., 2012; Wex et al., 2015). Yet the atmospheric variability in INP concentrations remains unresolved
88 (Hoose and Möhler, 2012; Kanji et al., 2017; Petters and Wright, 2015; Welti et al., 2018). In order to further quantify the
89 variability of INP responsible for ice formation in MPCs and increase the fundamental understanding of ice nucleation, we
90 developed and characterized the DRoplet Ice Nuclei Counter Zurich (DRINCZ), a drop freezing instrument to investigate ice
91 nucleation at temperature conditions between $-25\text{ }^{\circ}\text{C}$ and $0\text{ }^{\circ}\text{C}$, representative for MPCs. DRINCZ complements and extends
92 the INP concentration measurement capabilities of the single particle and bulk methods employed at ETH Zürich e.g. (Kohn
93 et al., 2016; Lacher et al., 2017; Lüönd et al., 2010; Marcolli et al., 2007; Stetzer et al., 2008). Furthermore, the automation of
94 DRINCZ and its portable design allows for the acquisition of INP data in the field and laboratory, ultimately increasing the
95 attainable information about the global distribution of INPs.



96 2 Instrument Design

97 DRINCZ is based on the design of Stopelli et al. (2014) and Hill et al. (2014). It consists of a temperature controlled ethanol
98 bath (Lauda ProLine RP 845, Lauda-Königshofen, Germany), a home-built LED light consisting of several LED light strips
99 enclosed in an ethanol proof housing, a home-built 96-well tray holder and camera mount, a webcam (Microsoft Lifecam HD-
100 3000) and a custom designed bath leveler, composed of a bath level sensor and valve (see Section 2.2) (Fig. 1a). The working
101 principle is similar to that of Stopelli et al. (2014), in that a USB camera detects the light transmission through aliquots of
102 sample. In DRINCZ, the aliquots are typically 50 μL and dispensed into a 96-well tray (732-2386, VWR, USA). To avoid
103 contamination, the top of the 96-well tray is sealed with a transparent foil (Axgen, Platemax CycloSeal Sealing Film, PCR-
104 TS). The webcam is programmed to take a picture every 15 seconds, which corresponds to a picture taken approximately every
105 0.25 $^{\circ}\text{C}$ decrease when the bath is cooled at a rate of 1 $^{\circ}\text{C min}^{-1}$. Moreover, both the picture frequency and cooling rate are
106 adjustable. Upon freezing, the light transmission through an individual well decreases (red circled well in Fig. 1b) due to the
107 polycrystallinity of the ice frozen in the wells.



108
109 **Figure 1: (a) Picture of DRINCZ. (b) Change in light transmission through the wells during an experiment with an example of an**
110 **unfrozen (blue circle) and frozen (red circle) well.**

111 The cooling cycle of the ethanol-based Lauda bath is controlled using LabVIEW® and the bath temperature is written to a text
112 file that is then read in by MATLAB® during the analysis. In addition, MATLAB® is also used to take and save the pictures
113 from the webcam. Both the LabVIEW® generated text file and pictures from the experiment are stored in the same folder for
114 data handling. A suite of MATLAB® functions have been written to automatically analyze and store the data from each
115 experiment, allowing for minimal user input (details of the code are provided in Appendix A) and rapid experiment throughput
116 of approximately 30 minutes per experiment and 2 minutes to process the data for frozen fraction as a function of temperature.



117 2.1 Detection Method

118 The ice nucleation detection in DRINCZ is achieved by the attenuation of visible radiation due to a frozen well compared to
119 transmission through a supercooled well. The images are analyzed by first detecting the pixels that correspond to each well of
120 the 96-well tray and then calculating the change of the average well brightness during an experiment between one picture and
121 the next. The well detection method is described in the following subsection, followed by the technique used to detect well
122 freezing.

123 2.1.1 Circular Hough Transform for Well Detection

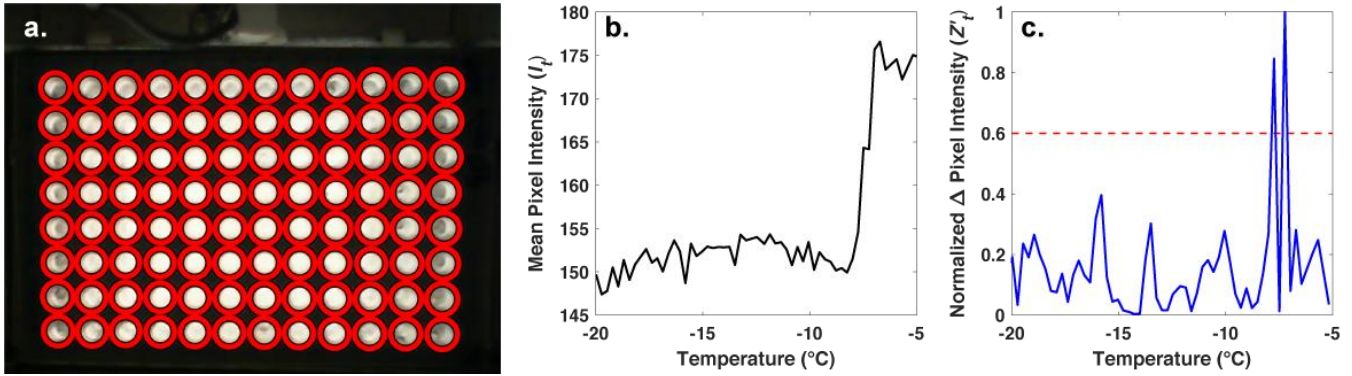
124 A fixed 96-well tray holder with an integrated webcam mount reduces variations in setting up the experiment. Nevertheless,
125 small changes in the location of the webcam due to mechanical shock during transport or testing, can produce misidentified
126 wells when algorithms rely on fixed well locations. Therefore, a freezing detection algorithm was developed to avoid errors
127 arising from small changes in the location of the wells. To optimize contrast, the PCR tray holder was constructed out of
128 aluminum so that light transmission only occurs through the wells (see Fig. A1). The high contrast between the illuminated
129 wells and dark tray holder allows for the automatic detection of the wells using a Circular Hough Transform (CHT) (e.g.
130 Atherton and Kerbyson, 1999). The CHT first identifies pixels along regions of large brightness gradients such as the pixels
131 at the edge of the well. To determine the center of each well, the algorithm draws circles of varying diameter all centered at
132 the edge of the well and classifies the pixel intersecting the largest number of circles as the well center. The radius of the well
133 is then given as the radius of the circles that led to the highest number of intersections. The pixels within a well are then
134 identified as the ones encompassed by a circle drawn from a well center with the calculated radius as denoted by the red circles
135 in Fig. 2a. Since the CHT identifies the well center locations in random order, they must be sorted based on their x and y
136 coordinates using a pixel scale for spatial biases or refreezing results to be analyzed. The wells are sorted based on their center
137 locations using the following equation:

$$138 \quad C_i = \frac{y_i}{D} L_x + x_i \quad (3)$$

139 where C_i is the value of the well center based on its pixel location in y and x coordinates, y_i and x_i , respectively, with the
140 origin taken as the pixel in the upper left hand corner of the image. L_x is the pixel number across the well array in the x



141 coordinate and D is the diameter (pixel number) of the wells. All the C_i values are then sorted to ensure that the wells are
 142 identified based on their location independent of the experiment.



143
 144 **Figure 2:** (a) Automatic detection of the wells (red circles) using a CHT. (b) Light intensity or I_t as a function of temperature as
 145 observed by the webcam and (c) the normalized change in pixel intensity, Z'_t , between pictures taken during an experiment, as a
 146 function of temperature. The dashed red line represents the 0.6 threshold required for a well to be classified as frozen.

147

148 2.1.2 Freezing Detection

149 With the well locations identified, the intensity values of the pixels within each well are averaged for each image recorded
 150 during an experiment (I_t). The change in I_t between subsequent images is used to identify the image where freezing occurred
 151 and the corresponding temperature (Fig. 2b). However, due to the slow freezing process which is limited by the latent heat
 152 release, the light transmission of a well continuously changes until the water is completely frozen as can be seen as two large
 153 peaks in Fig. 2c. To correctly identify the point in time when ice nucleation and not just freezing within the well occurs, the
 154 maximum change in I_t between subsequent images is normalized to 1 using the following procedure:

155 First, the Z-score (Z_t) of I_t is taken to level out differences in illumination within the 96-well tray:

$$156 Z_t = \frac{I_t - \mu}{\sigma} \quad (4)$$

157 where μ and σ are the mean and standard deviation of I_t for all recorded images of a well, respectively. The absolute value of
 158 the time derivative or the change in Z_t between subsequent images (dt) is given as:

$$159 Z'_t = \left| \frac{Z_t}{dt} \right| \quad (5)$$

160 Z'_t is then normalized to 1 by dividing by the maximum Z'_t of the well. The normalization ensures that a fixed threshold for the
 161 identification of ice nucleation can be used, independent of the absolute change in light transmission through a well during



162 initial freezing. Based on validation experiments, a threshold value of $0.6 \left(\frac{z'_t}{\max(z'_t)} \geq 0.6 \right)$ was found to be best for detecting
163 the initial freezing and to avoid assigning subsequent changes in transparency as a nucleation event due to slow freezing.

164 2.2 Bath Leveler

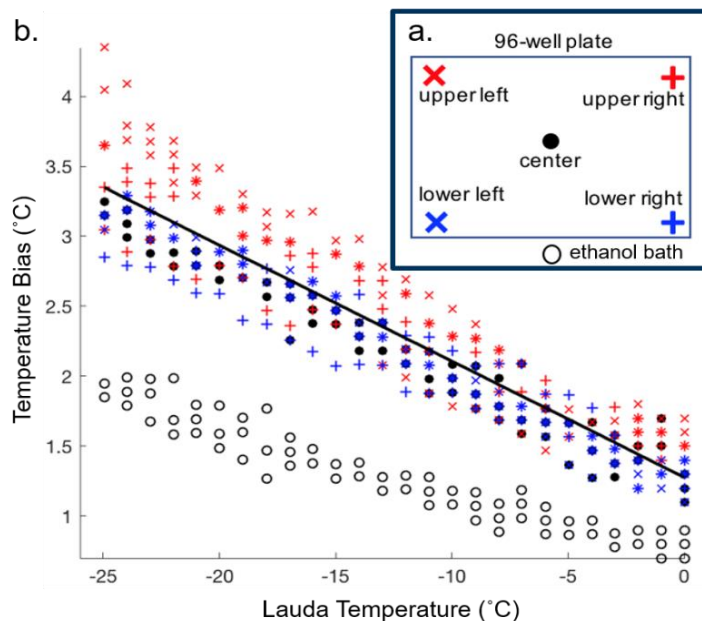
165 Due to the thermal contraction of the ethanol in the chilled bath between 0 and -30 °C, the ethanol level within the bath
166 decreases during an experiment, affecting the immersion level of the wells and thus the thermal contact. To keep the ethanol
167 level constant, a level sensor and solenoid valve are incorporated into the setup. The level sensor (Honeywell LLE 102101
168 liquid level sensor) detects when the ethanol falls below a fixed level relative to the wells and triggers the solenoid valve
169 (Kuhnke 64.025, 12 VDC valve) to open, allowing additional ethanol to flow into the bath. The level sensor and solenoid are
170 monitored and controlled using a ‘sketch’ written in Arduino (Arduino Uno Rev3 SMD). In order to minimize a possible
171 thermal gradient by adding warm ethanol to the bath, the ethanol is precooled to 0 °C using an ice water bath and then added
172 through a copper pipe that extends to the bottom of the bath. Thus, the bath leveler ensures that the wells remain in good
173 thermal contact due to a constant level of ethanol during experiments, while minimizing potential temperature fluctuations
174 within the bath. The resulting increased reproducibility of experiments due to the bath leveler is discussed in section 3.4.

175 3 Validation

176 The validation of the instrument is presented in four sections, with the first discussing the temperature calibration followed by
177 discussing the observed bias in freezing, the quantification of instrumental uncertainty and lastly, the improved reproducibility
178 of DRINCZ due to the addition of the bath leveller.

179 3.1 Temperature Calibration

180 The temperature reported as the freezing temperature is based on the ethanol bath temperature measured by the Lauda chiller
181 (T_{lauda}). In order to correct for the difference between the temperatures of the sample in the wells (T_{well}) and T_{lauda} , a temperature
182 calibration was performed. The calibration was conducted by measuring the temperature (Type K thermocouple) within the
183 four corner wells and a center well of the 96-well tray (Fig. 3a). The wells were filled with ethanol instead of water to extend
184 the calibration across the entire experimental temperature range of DRINCZ without the interference of freezing. The
185 temperature bias between the wells and T_{lauda} was measured every 1 °C while the bath was cooled at the typical ramp rate of
186 1 °C min⁻¹. The calibration was performed three times for each well (Fig 3b). Not surprisingly, we found that the ethanol
187 temperature in the bath was consistently lower than the temperature in the five calibration wells and the difference between
188 bath and well temperature increased linearly as the bath temperature decreased. Based on these results the linear function
189 $T_{\text{corr}} = 0.917 * T_{\text{lauda}} + 1.3$, with T_{lauda} in °C (black line in Fig. 3b) was derived to correct the well temperature, with a
190 maximum standard deviation of ± 0.6 °C.



191

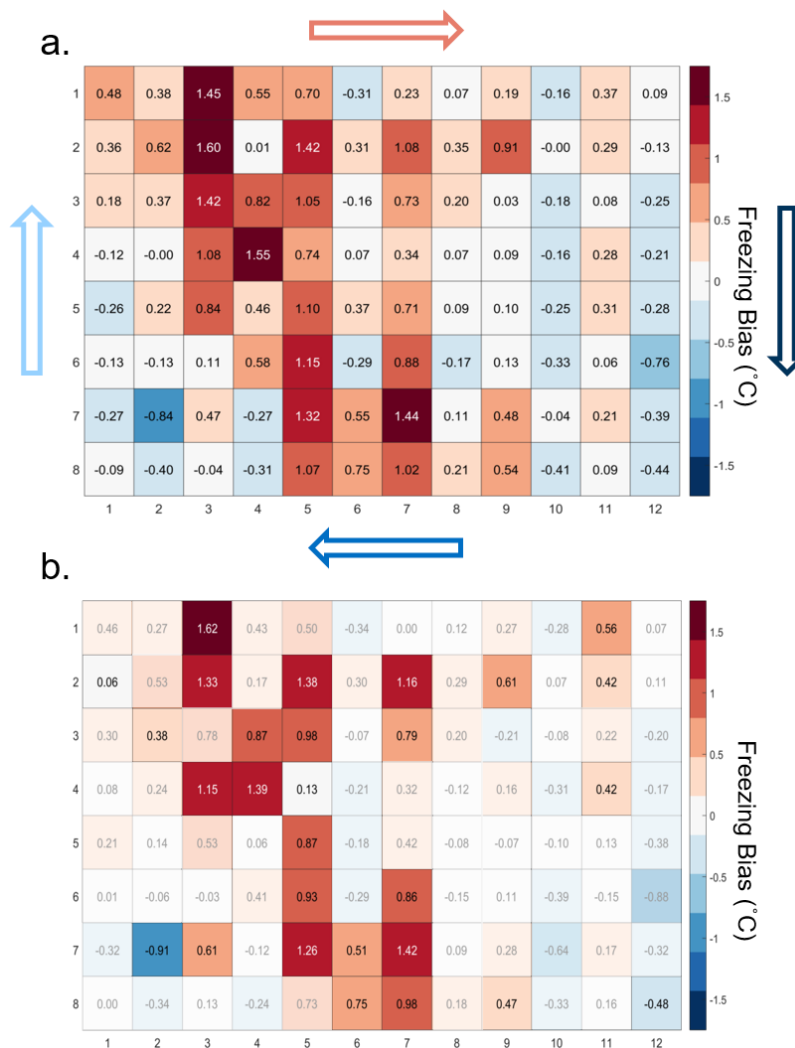
192 **Figure 3: (a) Locations of the type-K thermocouples tested during the temperature calibration. Additionally, the temperature**
193 **difference between the Lauda temperature and the ethanol bath was measured at the indicated location (black open circle).**
194 **The temperature bias between the wells and ethanol bath is displayed versus the Lauda bath temperature. The linear temperature**
195 **correction is shown in black.**

196 3.2 Freezing Bias across the 96-well Tray

197 The temperature calibration discussed above revealed potential variations in the well temperatures between the corner and the
198 center wells. We thus quantified the bias for individual wells, but conclude that it is within the instrument experimental error
199 as discussed below. To do so, 20 pure water (Molecular Biology Reagent, W4502 SigmaAldrich; hereafter referred to as SA
200 water) experiments were analyzed. SA water was chosen for this analysis due to its homogeneity and low freezing temperature,
201 where the observed spread in well temperature was maximized. For each well the median freezing temperature (or temperature
202 when frozen fraction (FF) = 50 %) (\tilde{w}_i) was compared to the median freezing temperature of the 4 corner wells (\tilde{w}_{4ref}) used
203 for the temperature calibration (see Fig. 3a). The difference between \tilde{w}_{4ref} and \tilde{w}_i ($\tilde{w}_{4ref} - \tilde{w}_i$) is shown in Fig. 4a. The red
204 (blue) shading indicates a warm (cold) bias and signifies that the solution in these wells are exposed to warmer (colder)
205 temperatures than the average of the four reference wells. The higher concentration of red shades in the middle of the tray
206 suggests that the center of the tray is exposed to as much as 1.5 °C warmer ethanol flow than the tray periphery. Indeed, the
207 ethanol circulates clockwise in the Lauda chiller and thus the freezing appears to track the flow (arrows in Fig. 4). Thus, the
208 ethanol circulation explains the observed bias. The same analysis procedure was applied to the same 20 samples separated by
209 user (12 and 8 experiments) and a similar bias was observed (see Appendix Fig. A2). Therefore, the reported bias is
210 instrumental, reproducible and any potential user bias can be excluded. The bias was found to be statistically significant at the
211 95% confidence interval for 30% of the wells and resulted in an overall bias of 0.23 °C (see Fig 4b and Appendix A.). As such,



212 a well by well bias correction was developed and tested as described in Appendix A. Although the bias correction performed
 213 as expected, the bias of 0.23 °C falls within the instrumental uncertainty as discussed in Section 3.3 and is therefore not applied
 214 to DRINCZ measurements by default. Nevertheless, the potential benefits and impacts of a bias correction is discussed in the
 215 following section.



216
 217 **Figure 4:** (a) Bias in the freezing of SA water ($\bar{w}_{4ref} - \bar{w}_i$ in °C) based on the median value of each well over 20 experiments relative
 218 to the median temperature of freezing for the 4 corner wells used during the temperature calibration. A positive (negative) bias
 219 indicates that the wells experience a warmer (colder) temperature than the four corner wells used for temperature calibration
 220 and therefore freeze at lower (higher) temperatures than reported. The arrows represent the ethanol circulation in the chiller and the
 221 color represents the temperature trend of the ethanol as it circulates in the bath with dark blue being the coldest and red the warmest.
 222 (b) Mean freezing bias of SA water between the four reference wells and each well ($\bar{w}_{4ref} - \bar{w}_i$). Positive (negative) values indicate,
 223 as denoted by shades of red (blue), wells that systematically freeze at colder (warmer) temperatures and therefore experience warmer
 224 (colder) temperatures than reported. Statistically insignificant biases as determined by a Welch's *t*-test (see Eq. A1) are depicted as
 225 greyed out.

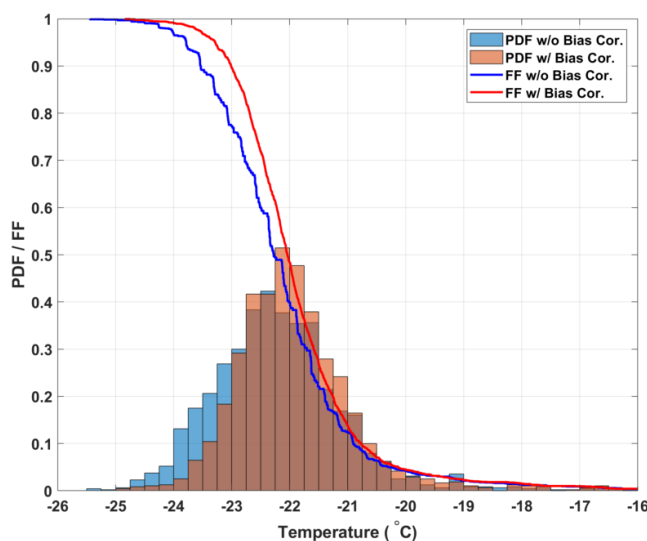


226 3.2.2 Impact of Bias Correction on Frozen Fraction

227 By accounting for the bias in freezing temperature across the 96-well tray by first applying the temperature calibration and
228 then the bias correction such that corrected well value (\bar{w}_i) becomes:

$$229 \bar{w}_i = \bar{w}_i + (\bar{w}_{4ref} - \bar{w}_i), \quad (6)$$

230 the slope of the FF curves steepens and becomes smoother, which is expected as the observed freezing temperatures become
231 more constrained (see Fig. 5). Although the median freezing temperature with and without the bias correction only changes by
232 0.2 °C (consistent with the correction of the mean bias of 0.23 °C found above), the narrowing of the freezing temperature
233 distribution is significant at the 95% significance level (Welch's t -test, see Eq. A1). This result shows that by using the spatial
234 dependent freezing information of a well from optically based drop freezing instruments like DRINCZ, temperature can be
235 better constrained. Such a bias correction should also be applicable to freezing methods that use block based cooling, where
236 gradients across the block may exist (Beall et al., 2017; Harrison et al., 2018).



237
238 **Figure 5: Histograms representing the probability distribution functions for freezing temperatures of the 20 SA water experiments**
239 **without (blue bars) and with the bias correction (red bars). The calculated cumulative distribution functions, or frozen fraction**
240 **curves without and with the bias correction are represented as the blue and red lines, respectively.**

241 242 3.3 Instrument Uncertainty

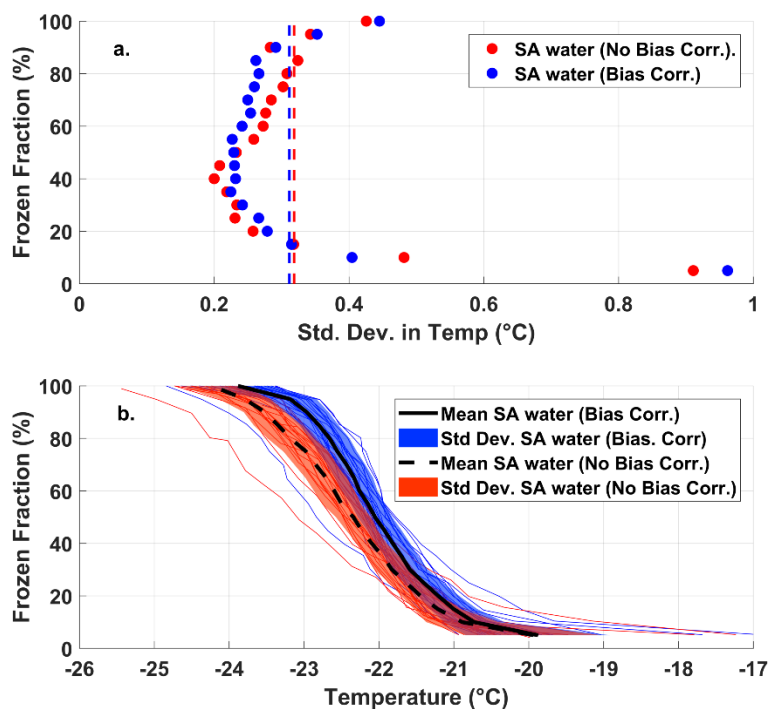
243 The instrumental uncertainty for DRINCZ is assessed by using the standard deviation in freezing temperature of the SA water
244 experiments in combination with the error in the temperature of the wells established during the temperature calibration. The
245 standard deviation of the freezing temperature of the SA water is dependent on FF , with a minimum at 50% FF (Fig. 6a). This
246 dependence is expected as the 50% FF corresponds to the most likely temperature for the SA water to freeze and therefore,
247 should show the least variability across the 20 experiments used in the analysis. The standard deviation at each FF is the



248 uncertainty due to the instrument as well as the variability in the freezing temperature of the SA water and represents the upper
249 limit of the instrumental uncertainty. Given the contribution to the uncertainty due to the variability of the freezing temperature
250 of the SA water, the standard deviation at $FF = 50\%$ can be used as the upper limit of the instrumental uncertainty across the
251 entire FF range. Incorporating a bias correction results in a negligible average difference in the standard deviation (as shown
252 by dashed lines in Fig. 6a). Thus, the upper limit of the instrumental precision is $\pm 0.3\text{ }^\circ\text{C}$ (the mean of the standard deviation
253 of freezing temperature over the entire freezing spectrum).

254

255 Although the instrumental precision indicates that DRINCZ is very reproducible ($\pm 0.3\text{ }^\circ\text{C}$), the accuracy in the reported
256 temperature must be accounted for. Based on the temperature calibration, the standard deviation of the well temperatures is
257 temperature dependent. At the coldest temperatures of the freezing range of the SA water ($\sim -25\text{ }^\circ\text{C}$), the standard deviation of
258 the well temperatures is largest, likely due to the increased gradient between the bath and air temperature and therefore, the
259 importance of the ethanol circulation through the bath is increased. To account for this temperature dependence, the maximum
260 standard deviation of $\pm 0.6\text{ }^\circ\text{C}$ from the temperature calibration, corresponding to the lowest observable freezing temperature
261 in DRINCZ (freezing temperature of SA water) is used. Therefore, when accounting for both the precision of the measurements
262 and the accuracy of the temperature, the overall uncertainty of the reported freezing temperature of a well in DRINCZ is
263 $\pm 0.9\text{ }^\circ\text{C}$. This value is comparable to other recently developed drop freezing techniques, which report uncertainties ranging
264 between $\pm 0.9\text{ }^\circ\text{C}$ (Harrison et al., 2018) and $\pm 2.2\text{ }^\circ\text{C}$ (Beall et al., 2017).



265

266 **Figure 6: (a) FF and the corresponding standard deviation of the freezing temperatures from the 20 SA experiments with and**
267 **without the bias correction shown as blue and red dots, respectively. The red and blue dashed lines represent the standard deviations**

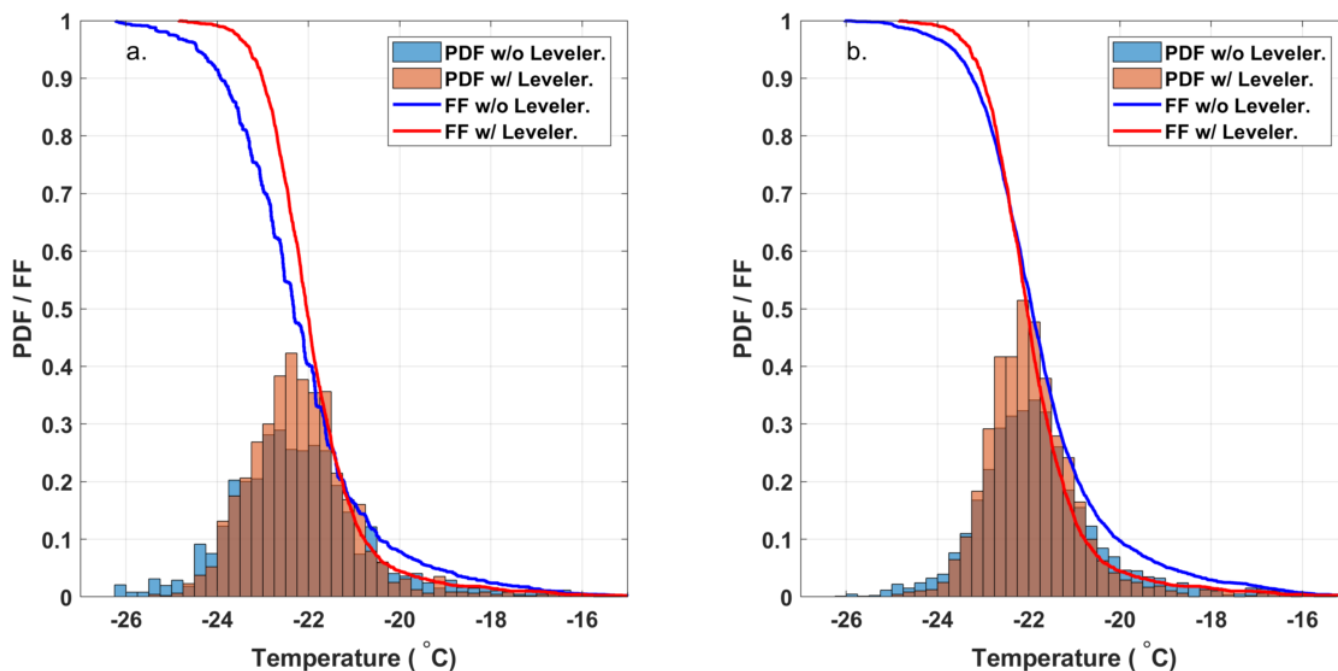


268 in temperature averaged over all FF values without and with the bias correction, respectively. (b) The FF of the 20 SA water
269 experiments as a function of temperature with and without the bias correction (thin blue and red lines, respectively). The color fill
270 represents the standard deviations of the SA water from the mean freezing temperature with (solid black line) and without (the
271 dashed black line) the bias correction.

272

273 3.4 Importance of the Bath Leveler

274 To assess the impact of the decreasing ethanol level on experiments in DRINCZ, 32 experiments with SA water without a bath
275 leveler were compared to the 20 SA water with a bath level sensor, the same 20 SA water discussed in the previous section.
276 Figure 7a shows that the bath sensor reduces the spread in freezing temperatures observed. The decrease in the 50 % FF
277 temperature without the bath leveler is due to a larger gradient between the aliquot and the bath temperatures, thus the well is
278 warmer than expected, requiring further cooling to observe freezing. The additional cooling in combination with the variable
279 starting level of the ethanol relative to the wells in the cases of no bath leveler is responsible for the longer freezing tail of the
280 FF curve (blue line) at higher FFs. Without the bath leveler, the initial height of ethanol relative to the wells is user dependent
281 and not reproducible, leading to both the higher and lower observed freezing temperatures.



282

283 **Figure 7: (a) Comparison of the freezing temperature of SA water without (32 experiments, blue) and with (20 experiments, red) the**
284 **bath leveler. The histograms are normalized to represent the PDF of the freezing temperatures and the lines represent the mean FF**
285 **curves of the SA water experiments. (b) Shows the same as panel a, except that a bias correction is applied to both sets of experiments.**

286 Although the median freezing temperature ($FF=50\%$) only decreased by $0.25\text{ }^{\circ}\text{C}$ without the bath leveler, the freezing curves
287 steepen when the bath leveler is incorporated in DRINCZ, leading to a decrease of the standard deviation from ± 1.4 to $\pm 1.0\text{ }^{\circ}\text{C}$
288 over the entire FF range. A bias correction applied following the procedure in Section 3.2 reduces the issues associated with



289 a variable bath level as seen by the similar FF curves and histograms normalized using the probability density function (PDF)
290 estimate in Fig. 7b for experiments with and without the bath leveler. The difference in mean freezing temperatures decrease
291 to 0.05 °C at $FF=50$ % and the standard deviation of the SA water freezing temperature without the leveler decreases from \pm
292 1.4 to \pm 1.2 °C over the entire FF range. This decrease is expected as the bias correction is designed to reduce the spread in
293 freezing temperatures within the 96 aliquots. Although the bias correction reduces the need for a bath leveler in DRINCZ, the
294 bias is instrument dependent and may be less pronounced in other drop freezing setups. Therefore, we recommend the use of
295 a bath leveler in any bath-based drop freezing devices.

296 4 Freezing Experiments

297 To verify the performance of DRINCZ in the context of other published drop freezing techniques, we use the SA water
298 experiments to characterize the instrumental background (Section 4.1) and perform freezing experiments with NX-illite
299 suspensions (Section 4.2). To demonstrate applicability of the instrument to analysis of field samples, the evolution of the ice
300 nucleating ability of atmospheric aerosol particles collected in snow samples at the Sonnblick Observatory in the Hohe Tauern
301 region of Austria during a mid-latitude storm system is assessed in Section 4.3. Lastly, some uncertainties associated with
302 measuring INP in snow samples (Section 4.4) and further validation of DRINCZ through dilutions are discussed (Section 4.5).
303

304 4.1 Background of DRINCZ

305 The background freezing due to the experimental technique and the SA water used to suspend and dilute samples must be
306 known to discriminate freezing events due to the sample from freezing events due to the water used. The 20 SA water
307 experiments are therefore used to assess the instrument background freezing. It is important to note that in cases where solvents
308 other than SA water are used or where contamination from a sampling technique (e.g. snow collection or impinger
309 measurements) is possible, a different background calculation must be used to accurately assess the freezing ability of a sample.
310 The background of DRINCZ when used with SA water, is calculated by fitting the 20 SA water experiments with a five
311 parameter Boltzmann fit. The five parameter version was chosen to account for asymmetry (Spiess et al., 2008) in the freezing
312 of the SA water but due to the minimum and maximum values of FF given as 0 and 1, respectively, the fit reduces to three
313 parameters and takes the form:

$$314 \quad FF_{BGfit}(T_{frzBG}, a, b, c) = \frac{1}{\left(1 + e^{a(T_{frzBG} - b)}\right)^c}, \quad (8)$$

315 where FF_{BGfit} is the fitted FF of the SA water as a function of the observed freezing temperatures of the SA water, T_{frzBG} ,
316 and the fitting parameters, a , b , c represent the slope of the fit ($a = 1.9651$), the inflection point ($b = -22.7134$) and the
317 asymmetry factor ($c = 0.6160$), respectively. The value of 1 in the numerator represents the maximum FF . The fit and
318 associated coefficients (including 95% confidence range and r^2) are shown in Table 1 and Fig. 8 respectively.



319

320 **Table 1: Coefficients for the three parameter Boltzmann fit of the SA water freezing background and 95th percentile confidence**
 321 **interval bound values.**

	a	b	c	r^2
Best	1.9651	-22.7134	0.6160	0.97
-95 th %	1.7254	-22.8955	0.4683	N/A
+95 th %	2.2049	-22.5312	0.7637	N/A

322

323 The fitted freezing background is used to correct for the contribution of SA water to the observed freezing of a sample. To
 324 account for the presence of multiple ice nucleating particles coexisting in a single well, the background is removed by
 325 subtracting the differential nucleus concentration of the background from that of the sample (Vali, 1971, 2019). The differential
 326 nucleus concentration ($k(T)$) is initially defined in Vali (1971) as:

$$327 \quad k(T) = -\frac{1}{V_a \Delta T} \cdot \ln \left(1 - \frac{\Delta N}{N(T)} \right), \quad (9)$$

328 where $N(T)$ is the number of unfrozen aliquots at the beginning of a temperature step while ΔN is the number of aliquots that
 329 freeze during the temperature step (between pictures) or ΔT .

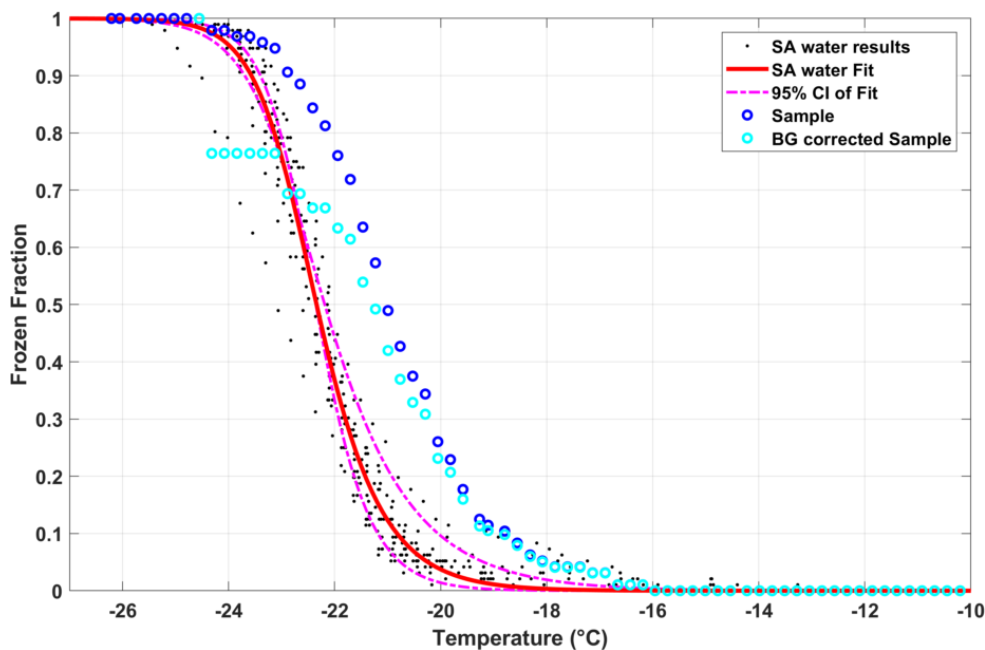
330 The background corrected differential nucleus concentration ($k_{corr}(T)$) is obtained by:

$$331 \quad k_{corr}(T) = k_{sam}(T) - k_{bg}(T), \quad (10)$$

332 where $k_{sam}(T)$ and $k_{bg}(T)$ are the sample and background differential nucleus concentration, respectively. The background
 333 corrected $FF_{cor}(T)$ is then achieved by inverting Eq. 9 and taking the cumulative sum of $k_{corr}(T)$:

$$334 \quad FF_{cor}(T) = 1 - \exp(-\sum[k_{corr}(T) \cdot \Delta T] \cdot V_a), \quad (11)$$

335 An example of the impact of the background correction on the FF of the diluted snow sample collected on Nov 30th 2017
 336 (discussed in section 4.3) is shown in Fig. 8.



337
 338 **Figure 8:** SA water data (black dots) and corresponding fit (red line, Eq. 8) including the 95th percentile confidence interval (dashed-
 339 dot magenta lines). The blue circles represents the diluted snow sample collected on Nov 30th 2017 which is then corrected for the
 340 contributions of freezing from the SA water using the background correction ($FF_{cor}(T)$) as described in Eq. 11; cyan circles).

341
 342 **4.2 Comparison of DRINCZ to other immersion freezing techniques**

343 To validate the performance of DRINCZ, we use different wt. % NX-illite suspensions to compare the results from DRINCZ
 344 to those summarized in Hiranuma et al. (2015), Beall et al. (2017) and Harrison et al. (2018). In the atmosphere, illite constitutes
 345 up to ~40 % of the transported dust fraction (Broadley et al., 2012; Murray et al., 2012), making it an excellent surrogate for
 346 atmospherically relevant dust. Three mass concentrations of NX-illite (0.01, 0.05, and 0.1 wt. %) were investigated with
 347 DRINCZ (see Fig. A4 for FF curves) and then normalized to the number of active sites per BET-derived surface area (n_{sBET})
 348 using a variation of Eq. 2 as follows:

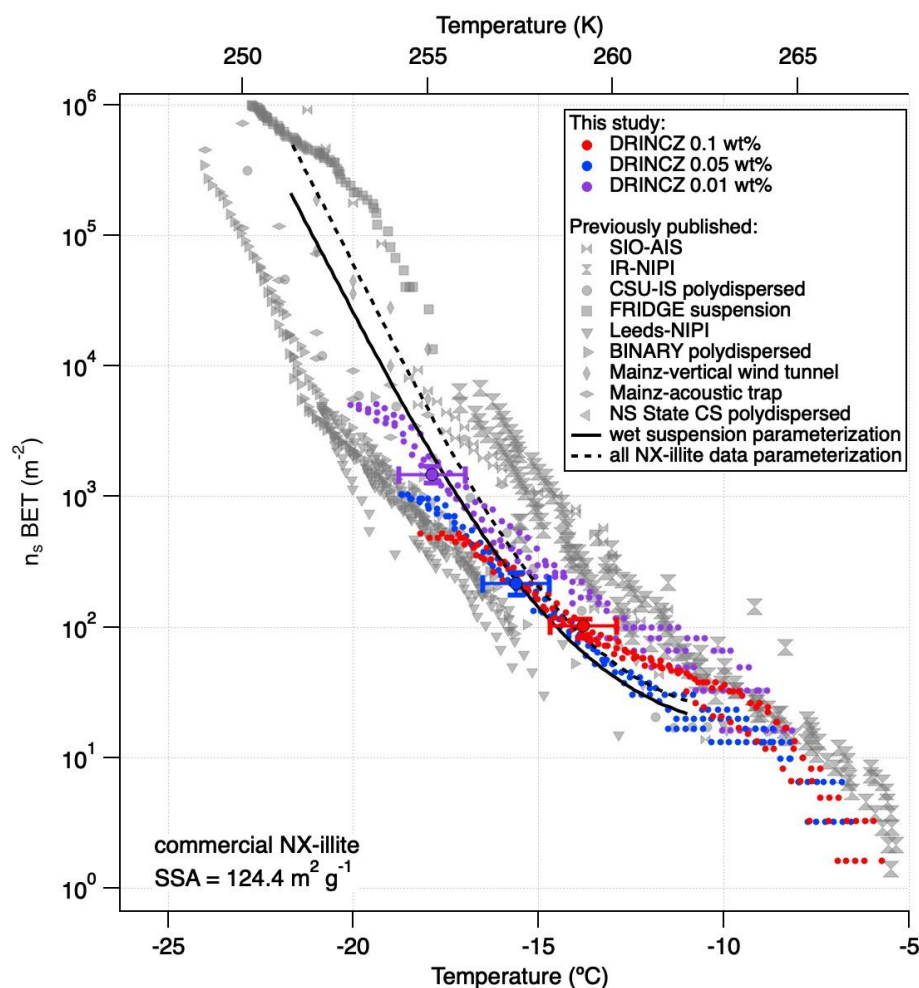
349
$$n_{sBET} = - \frac{\ln(1-FF)}{V_a * SA_{BET} * C_{NX}}, \quad (12)$$

350 where SA_{BET} is the BET surface area of the particles used (NX-illite) and C_{NX} is the mass concentration of NX-illite in an
 351 experiment.

352
 353 The n_{sBET} of NX-illite calculated using Eq. 12 from the measurements made with DRINCZ falls within the results from
 354 Hiranuma et al. (2015), Beall et al. (2017) and Harrison et al. (2018) (Fig. 9). In theory, n_{sBET} should be insensitive to
 355 concentration as the number of ice nucleating sites is normalized to the total surface area. Indeed, the differing weight percent
 356 samples overlap (Fig. 9). Furthermore, the lower-weight-percentage samples extend the observable n_{sBET} to higher values and



357 colder temperatures, as expected. Similar to the observations of Harrison et al. (2018), a few of the data points from the
358 0.01 wt. % solution appear as outliers at the warmest temperatures. This is likely due to an uneven distribution of the active
359 sites in each aliquot and may be the result of diluting a single stock solution rather than producing individual weight percent
360 solutions (Harrison et al., 2018). Thus a spread equivalent to or less than the spread in the concentrations, up to an order of
361 magnitude in this case, can be expected. Furthermore, when accounting for the $\pm 0.9^\circ\text{C}$ uncertainty, depicted by the horizontal
362 error bars, the results between concentrations become more similar and fall within the same range as the measurements of
363 Beall et al, (2017) who used similar concentrations of NX-illite. The overlap between the n_{sBET} measured with DRINCZ and
364 the NX-illite parameterization (Hiranuma et al., 2015) indicate that DRINCZ is capable of accurately measuring the
365 concentration of INPs and their active sites in the immersion freezing mode (Fig. 9).



366
367 **Figure 9:** n_{sBET} of three concentrations of NX-illite, 10^{-3} g ml^{-1} (red dots), $5 \times 10^{-4}\text{ g ml}^{-1}$ (blue dots) and 10^{-4} g ml^{-1} (purple dots), are
368 measured as triplicates by DRINCZ and reported as a function of temperature. An example of the temperature uncertainty and the
369 uncertainty due to the background correction are depicted for each weight percent as horizontal and vertical error bars, respectively.
370 Literature values from Hiranuma et al, (2015), Beall et al, (2017) and Harrison et al, (2018) are shown for comparison. n_{sBET} was
371 calculated using a BET surface area of $124.4\text{ m}^2\text{ g}^{-1}$ (Hiranuma et al., 2015).



372

373 4.3 Ice Nucleating Particle Concentrations in Snow Samples from a Mountaintop Observatory in Austria

374 In order to demonstrate the performance of DRINCZ, snow samples collected between the 27th and 30th of November 2017 at
375 the Sonnblick Observatory (SBO) were analyzed. The SBO is located at 3106 m on the summit of Mt. Sonnblick in the Hohe
376 Tauern Region of Austria and has previously been used for cloud microphysical measurements (e.g. Beck et al., 2018;
377 Puxbaum and Tschewenka, 1998). Freshly fallen snow was collected from a wind-sheltered area where the snow could not
378 drift. A stainless steel shovel (Roth) was conditioned with snow by turning (10 times) in the surface snow next to the sampling
379 site prior to sampling. The snow was then sampled into sterile NascoWhirlPaks (Roth) and then melted at room temperature
380 (20 °C), immediately after which aliquots of snow-meltwater were filled into sterile centrifugation tubes (15 ml, Falcon tubes)
381 and stored at -20 °C. The samples were stored frozen until processed with DRINCZ to avoid any bacterial growth or changes
382 due to liquid storage (Stopelli et al., 2014). The snowfall collected at SBO occurred during two snowfall events. The first event
383 began on the 25th and ended overnight on the 26th (early hoursth of the 27th) while the second event (28th -30th) was associated
384 with an intensifying upper level trough, a developing surface cyclone, a strong cold front and an associated secondary low (see
385 Fig. A5 and A6).

386

387 The frozen fractions of five different snow samples were determined using DRINCZ and the cumulative concentration of
388 active sites (or $INP(T)$, see Eq. 1) were normalized to per L of meltwater (n_{mw}) (Fig. 10). Overall, the n_{mw} of the snow samples
389 fall within the range of previously reported values for precipitation samples (Petters and Wright, 2015) except for the
390 November 30th sample. Within these samples, we identify (1) a particularly active snow sample (Nov 28th), (2) samples having
391 intermediate IN activity (Nov 27, 29), and (3) a least active sample (Nov 30th). We attempt to compare these snow samples
392 based on their air mass origin.

393

394 The snowfall sampled on the 28th had the highest n_{mw} of all collected samples (Fig. 10). The meteorological conditions and a
395 comparison of back trajectories indicate that the air mass was associated with the warm sector of a synoptic system (Fig. A7)
396 that originated from North America and the North Atlantic that then crossed France and Switzerland, before arriving at SBO
397 (Fig. A8). In contrast, the arctic air mass responsible for the snowfall sampled on the 27th originated over Svalbard before
398 crossing Iceland, the British Isles, Northern France and Germany (Fig. A8).

399

400 Even though the local conditions at SBO did not change significantly between the 28th and 29th, a decrease in n_{mw} was observed
401 relative to the 28th and n_{mw} gradually decreased between the first and second sample on the 29th (Fig. 10). The back trajectories
402 show that the origin of the air mass changed from North America and the North Atlantic on the 28th to exclusively originating
403 over the North Atlantic on the 29th (Fig. A8). Additionally some of the back trajectories on the 29th show an increased
404 interaction with the boundary layer over Europe (Fig. A8). Nevertheless, the decrease in n_{mw} suggests that if boundary layer



405 aerosols from parts of Europe did reach the precipitating clouds at the SBO, they are less efficient INPs than the marine aerosols
406 (Lacher et al., 2017, 2018) associated with the samples on the 27th and 28th.

407

408 Finally, the lowest n_{mw} observed were from meltwater collected on the 30th. The cold frontal passage and associated cold air
409 advection caused the temperature to drop by 6 °C by noon on the 30th (Fig. A7) and the n_{mw} in the associated snowfall decreased
410 substantially, exceeding the lower limit of previously reported n_{mw} values (Petters and Wright, 2015, Fig. 10). The decrease in
411 n_{mw} , however, cannot be explained solely on the origin of the air mass as the arctic air mass on the 27th also crossed similar
412 parts of the UK or had significant interaction with the marine boundary layer. Nevertheless, the concentration of INPs in the
413 sea surface microlayer is variable and the efficiency of emitting marine INP from the surface is wind speed dependent (DeMott
414 et al., 2016; Irish et al., 2017; McCluskey et al., 2018; Wilson et al., 2015). Therefore, even though the trajectories on the 27th
415 and 30th interacted with the marine boundary layer, they may contain different concentrations of INPs, yielding the observed
416 differences in n_{mw} . In addition to air mass origin, it has been shown that precipitation efficiently removes INP and thus
417 influences n_{mw} (Stopelli et al., 2015). Indeed, the most upstream precipitation (see Fig. A8) corresponds to the sample collected
418 on the 30th, which has the lowest n_{mw} . Therefore, the most efficient INPs could have been removed in the upstream
419 precipitation, contributing to the observed decrease in n_{mw} .

420

421 The differences in n_{mw} could not be rectified by a single metric in this study but rather a combination of factors likely led to
422 the observed variability. In particular, as the warm sector of the cyclone approached the sampling site (28th), n_{mw} increased.
423 Conversely, after cold frontal passage (30th) the n_{mw} decreased. Back trajectories indicate that the air mass source region and
424 the amount of upstream precipitation differed between the two sectors of the cyclone. This result is consistent with previous
425 studies that suggest that air mass origin (e.g. Ault et al., 2011; Creamean et al., 2013; Field et al., 2006; Lacher et al., 2017,
426 2018) and upstream precipitation (Stopelli et al., 2015) influences the INP concentration. Furthermore, the dependence on the
427 long range air mass history to the observed variability in n_{mw} suggests that local sources are not responsible for the observed
428 INPs.

429 **4.4 Limitations of snow meltwater sample comparisons**

430 One limitation when comparing snow samples collected at different times and locations is the unknown number of aerosols,
431 INPs and ice crystals that contributed to the collected meltwater. Since n_{mw} depends on the number and mass of the ice crystals
432 within a snow sample, the melt water volume or density of each snowflake influences n_{mw} . For example, snow to liquid ratios,
433 which can be used as a proxy for snow flake density and melt water equivalent, can vary between 5 to 1 in heavy wet snow
434 and 100 to 1 in powdery snow (Roebber et al., 2003). However, even when considering this variability in the required amount
435 of snow to produce the same volume of ice crystal melt water, n_{mw} would only differ by a factor of 20. As can be seen in
436 Fig. 10, n_{mw} varies by two orders of magnitude or more between the 28th and the 30th of November and the difference is
437 therefore robust. Additionally, heavy wet snow has been found to occur in the warm core of a synoptic system while lighter,

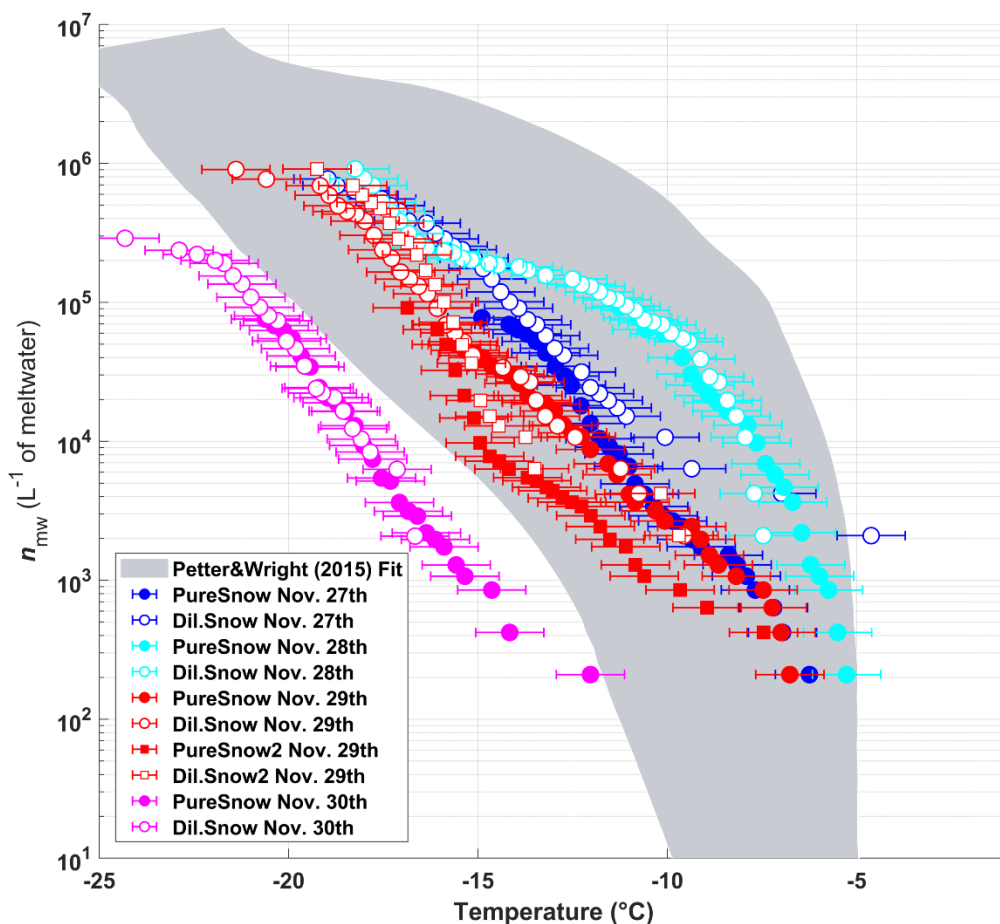


438 more powdery snow was found in the air mass after cold frontal passage, where air temperatures are colder (Roebber et al.,
439 2003). As the n_{mw} on the 28th was collected in the warm sector and the sample on the 30th was post cold front, differences in
440 snow density may lead to an underestimation in the difference between the n_{mw} of these two samples. Therefore, we recommend
441 that future studies also consider the snow water equivalent when comparing the n_{mw} as this could influence n_{mw} by a factor of
442 20 or more.

443
444 Another uncertainty with using precipitation samples for analyzing INP concentrations is associated with aerosol scavenging
445 and chemical ageing (e.g. (Petters and Wright, 2015). As previously mentioned, the samples were stored frozen to avoid any
446 decrease in ice nucleating ability associated with storage (Stopelli et al., 2014) and therefore degradation is likely not an issue
447 in this study (Wex et al., 2019). The ability of a falling ice crystal to scavenge aerosols or rime cloud droplets depends on the
448 ice crystal habit, size, and the difference between the fall velocity of the crystal and the interstitial aerosol or cloud droplets.
449 With the exception of interstitial aerosol concentration which has been shown to influence n_{mw} by a factor of 2 (Petters and
450 Wright, 2015), these factors are all important when estimating snow density and thus make it difficult to disentangle their
451 effects on n_{mw} . Therefore, there is value in future studies of INP in MPCs to investigate the INP concentrations in cloud water,
452 interstitial aerosols and snow samples.

453 **4.5 Ice Nucleating Particle Concentrations in Diluted Snow Samples**

454 In order to extend the reported temperature range of DRINCZ, the snow samples were also diluted by a factor of 10 with SA
455 water (see Eq. 2). The dilutions (open symbols) overlay the pure samples except at the warmest temperatures where, as
456 previously mentioned, a single freezing event can lead to an increase in n_{mw} of an order of magnitude relative to the undiluted
457 sample. This effect is especially evident on the 27th when the first few wells of the diluted sample (open blue circles) froze at
458 the same or higher temperatures than the undiluted sample (filled blue circles) and led to an increase in n_{mw} of up to an order
459 of magnitude. However, this issue has been previously observed when diluting from stock solutions (Harrison et al., 2018)
460 which is similar to diluting a snow water sample. Therefore, the dilutions further validate DRINCZ as an INP measurement
461 technique.



462

463 **Figure 10:** The cumulative number of active sites per L of meltwater (n_{mw}) of snow for undiluted snow (filled) and of snow samples
464 diluted by a factor of 10 (white-filled symbols) as a function of temperature. The colors represent the different sampling days. On
465 the 29th of Nov. two samples were taken and the second sample of the day is indicated by square symbols. The shaded area represents
466 the previously reported n_{mw} from precipitation events as described in Petters and Wright (2015). The error bars represent the
467 instrumental temperature uncertainty of ± 0.9 °C.

468 5 Conclusions

469 We describe and characterize DRINCZ as a newly developed drop freezing instrument for quantifying the ability of aerosols
470 to act as ice nucleating particles in the immersion freezing mode. The instrument uncertainty is ± 0.9 °C, similar to previously
471 published drop freezing techniques. We show that thermal contraction of ethanol as a coolant used in bath-based drop freezing
472 techniques increases temperature variations within the sample. This issue can be corrected by incorporating a bath leveler
473 which ensures the coolant level in the bath remains constant during an experiment. Typical drop freezing methods report
474 temperature measured in the corner wells of a 96-well tray, at the edge of a cooling block or within the block itself (Beall et
475 al., 2017; Hill et al., 2014; Stopelli et al., 2014). Here we show that by making use of the freezing sequence of pure water
476 aliquots, the spatial pattern of temperature bias in the 96-well tray can be assessed. Although variations are within the



477 instrumental uncertainty of DRINCZ and are not used for DRINCZ data analysis, we present our detailed analysis of this
478 potential bias and draw attention to this issue for other drop freezing techniques. The calculated bias correction increases the
479 precision of drop freezing setups, and is an alternative to computationally expensive heat transfer simulations (Beall et al.,
480 2017). Validation experiments conducted with NX-illite showed good agreement with data reported in the literature for this
481 INP standard.

482
483 We exemplify the use of DRINCZ by measuring the concentration of INP in snow samples collected at the Sonnblick
484 Observatory in Austria. The observed INP concentrations are within previously reported values as summarized in Petters and
485 Wright, (2015) for the same temperature range as investigated here (-22 to 0 °C). Differences in INP concentration can be
486 explained by differing sectors of a mid-latitude cyclone. As the warm sector of the cyclone approached the sampling site, the
487 INP concentration increased while after the cold front passed the INP concentration decreased. Back trajectories indicate that
488 the air mass source region and the amount of upstream precipitation differed between the two sectors of the cyclone. This
489 result is consistent with previous studies that suggest that air mass origin (e.g. (Ault et al., 2011; Creamean et al., 2013; Field
490 et al., 2006; Lacher et al., 2017) and upstream precipitation (Stopelli et al., 2015) influence the INP concentration. This suggests
491 that INP in precipitation samples are likely transported from specific source regions rather than originate from local sources.
492 Thus identifying the specific sources responsible for INP and their transport pathways are essential for accurately modelling
493 the ice phase in clouds and ultimately, climate.

494

495 **Author Contributions**

496 DRINCZ was developed and designed by R.O.D with the assistance of M.C.C, M.R., L.S.B, K.P.B and N.B.D. The SA water
497 experiments were conducted by M.C.C, K.P.B., L.S.B, V.W, J.W, S.B, and R.O.D. The temperature calibration and NX-illite
498 experiments were conducted and analyzed by K.P.B and N.B.D. The snow samples were collected by N.E. and analyzed by
499 R.O.D. The instrumental error, uncertainties and calibration were conducted by R.O.D. with contributions from Z.A.K and
500 C.M. The automation and analysis software was developed by R.O.D. with contributions from K.P.B and M.C.C. The well
501 plate holder was designed by M.R. and R.O.D. and manufactured by M.R. The manuscript was written by R.O.D with
502 contributions from N.B.D, C.M. and Z.A.K. The project was supervised by Z.A.K.

503

504 **Acknowledgements**

505 R.O.D. and Z.A.K. would like to acknowledge funding from SNF grant #200021_156581. Z. A. K. would like to acknowledge
506 Franz Conen and Emillano Stopelli for assistance with the initial set up of the droplet freezing assay. We are grateful to Dr.



507 James D. Atkinson for discussions and help with experiments during the preparatory phase of DRINCZ development. We
508 acknowledge technical assistance from Hannes Wylder. R.O.D. would like to thank Dr. William Ball for insightful statistical
509 discussions, Ellen Gute for performing camera tests and Michele Gregorini for assistance with the automation.

510 **Appendix A**

511 **Freezing bias by user**

512 The 20 SA water experiments were performed over a three month period by two users. The SA water was unaffected by aging
513 over this period as it originated from varying bottles distributed by the manufacturer (Sigma Aldrich). The user bias was
514 calculated the same way as the bias for all 20 experiments. The bias is relative to the median freezing temperature of the 4
515 corner wells obtained by the respective user. As can be seen in Fig. A2, the pattern of freezing bias is consistent regardless of
516 the user. This similarity indicates that the reported bias is instrumental and not user specific.

517

518 **Bias significance and correction**

519 To ensure that the observed bias is statistically significant, a two-sample, two-tailed t -test was performed. In particular, a
520 Welch's t -test was used due to the different number of samples between the combination of the 4 reference wells (20
521 experiments \times 4 wells = 80 values) and each well (20 experiments \times 1 well = 20 values) and the different variance of freezing
522 for each well (Derrick and White, 2016). In a Welch's t -test the location parameter of two independent data samples is assessed
523 as follows:

$$524 \quad t = \frac{\bar{w}_{4ref} - \bar{w}_i}{\sqrt{\frac{s_{4ref}^2}{Nw_{4ref}} + \frac{s_i^2}{Nw_i}}} \quad (A1)$$

525 where \bar{w}_{4ref} and \bar{w}_i are the mean freezing temperature of the reference wells and an individual well, respectively. s_{4ref}^2 and
526 s_i^2 are the variances of freezing in the reference and the individual wells and Nw_{4ref} and Nw_i are the number of samples for
527 the reference wells and an individual well, respectively. The variance of the freezing temperature of SA water in each well is
528 shown as boxplots in the Appendix (Fig. A3). The temperature of approximately 30% of the wells was found to be statistically
529 different from the average freezing temperature of the 4 reference wells at the 95% confidence level, with a resultant mean
530 bias of 0.23 °C (Fig. 4b). Due to a fraction of wells with a statistically significant bias, a correction factor based on the mean
531 bias from the 20 SA water experiments is tested for all wells excluding the 4 corner wells used as the reference to avoid
532 overfitting the data. Of note, the reported bias is derived based on the freezing range of SA water from -16 to -26 °C. However,
533 based on the relatively constant spread in the temperature calibration data (see Fig. 3b), it is reasonable to assume that the bias
534 has a weak temperature dependence.



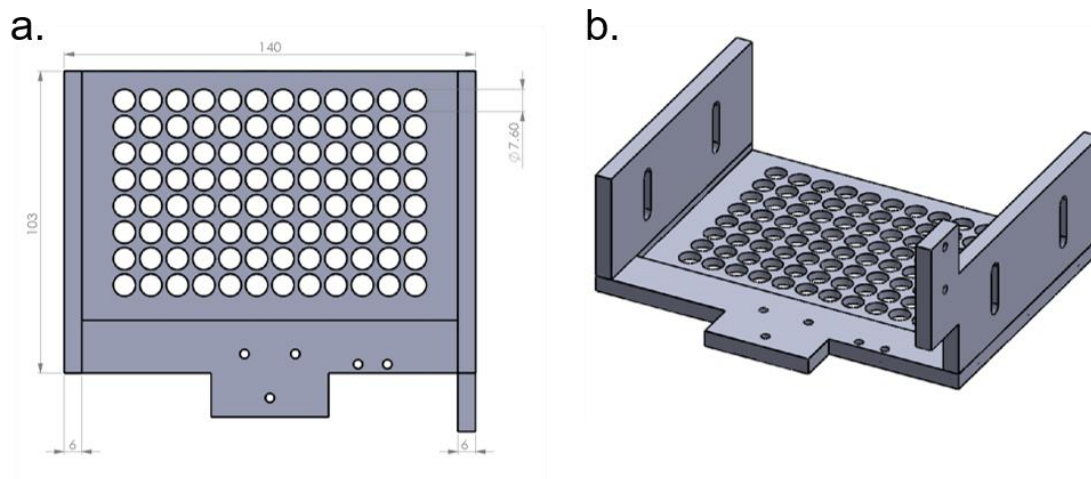
535 Although the freezing bias was shown to be representative when the SA water data was split in two (8 and 12 samples), it is
536 still necessary to validate its robustness on a larger sample size. In order to artificially increase the sample size of the
537 experiments, the bias was recalculated randomly such that only 90% or 18 of the experiments were used. The resultant bias
538 correction was then applied to the remaining 10% or 2 of the experiments and tested to see if the mean freezing temperature
539 of the bias corrected tray was closer to the reference freezing temperature of the 4 corner wells. This procedure was repeated
540 1000 times at random. The difference in the median freezing temperature (FF= 50 %) and 4 corner reference wells decreased
541 from 0.23 °C to 0.04 °C, while the standard deviation of the bias corrected data increased by 0.007 °C. Thus, the bias correction
542 performed as expected and reduced the bias in freezing temperature. Nonetheless, this improvement falls within the uncertainty
543 of the instrument, as discussed in Section 3.3 and is therefore not applied to DRINCZ measurements by default.
544

545 **Synoptic Summary Nov. 27th-30th**

546 The synoptic pattern over Europe on the 27th through 30th of November produced large variations in both temperature and air
547 mass origin at the SBO. As can be seen from the surface pressure maps shown in Fig. A5, an evolving cyclone tracked across
548 Northern Europe before occluding in the vicinity of Denmark. This cyclone produced strong warm advection at SBO on the
549 27th (see Fig. A7) in advance of the approaching cold front. As the cyclone began to fill over Southern Scandinavia, the cold
550 front stalled along the Alps and westerly flow continued at SBO from the 28th – 29th (Fig. A7). Farther west, the cold front
551 reached the Mediterranean where a secondary low developed along the remnant baroclinic zone (Fig. A6 panel c.). This
552 secondary low traversed Italy and rapidly intensified as it crossed the Adriatic Sea before entering the northern Balkans (Fig.
553 A6 panel d.). The secondary low and an amplifying ridge over the British Isles forced the cold front over SBO at 00Z on the
554 30th when cold air advection ensued over the SBO region (Fig. A7), as shown by the back trajectories (Fig. A8.e and f.).

555 **HYSPLIT back trajectories**

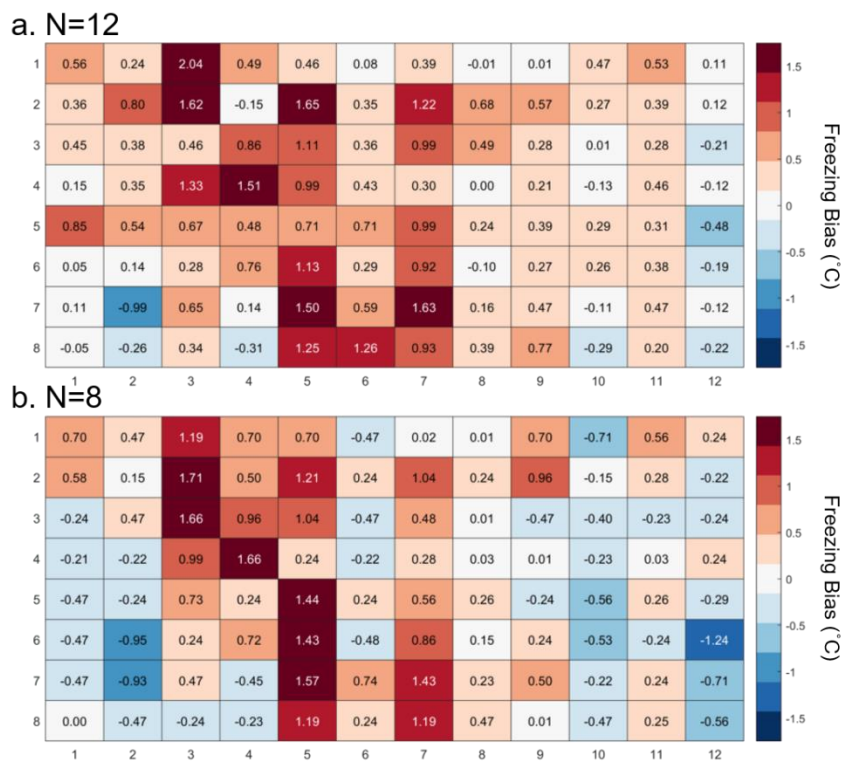
556 The Hybrid Single-Particle Lagrangian Integrated Trajectory model (HYSPLIT) (Stein et al., 2015) was run using the
557 interactive web portal (Rolph et al., 2017). The trajectories were calculated using 0.5° resolution and the trajectories were
558 initialized 1000, 2000 and 3000 meters above the model terrain height. Although the majority of snow mass growth has been
559 shown to occur between mountaintop and 1 km above the surface (Lowenthal et al., 2016), these heights were chosen due to
560 the coarse resolution of the model terrain height and the observed sensitivity of the back trajectories with height. HYSPLIT
561 was initialized using the 0.5° hourly Global Data Assimilation System (GDAS) archived database and the vertical velocity was
562 model based rather than isentropic.



563

564 **Figure A1:** Schematic of the 96-well tray holder from above (a) and the side (b), dimensions are in millimeters.

565

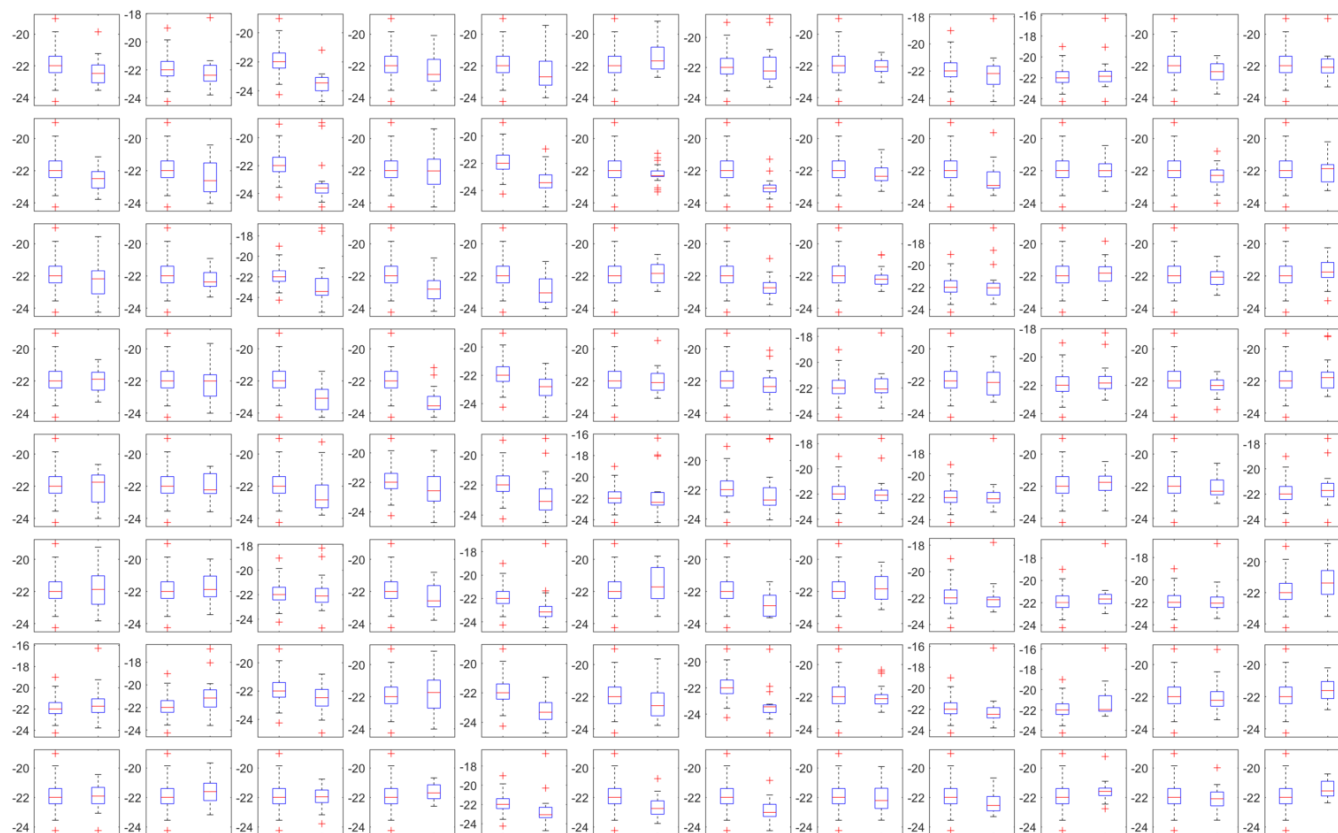


566

567 **Figure A2:** (a) Bias in the freezing of SA water ($^{\circ}\text{C}$) based on the median value of each well over 12 experiments and (b) 8 experiments
 568 relative to the median temperature of freezing for the 4 corner wells used during the temperature calibration. A positive (negative)
 569 bias indicates that the wells experience a warmer (colder) temperature than the four corner wells used for temperature calibration
 570 and therefore freeze at lower (higher) temperatures than reported.

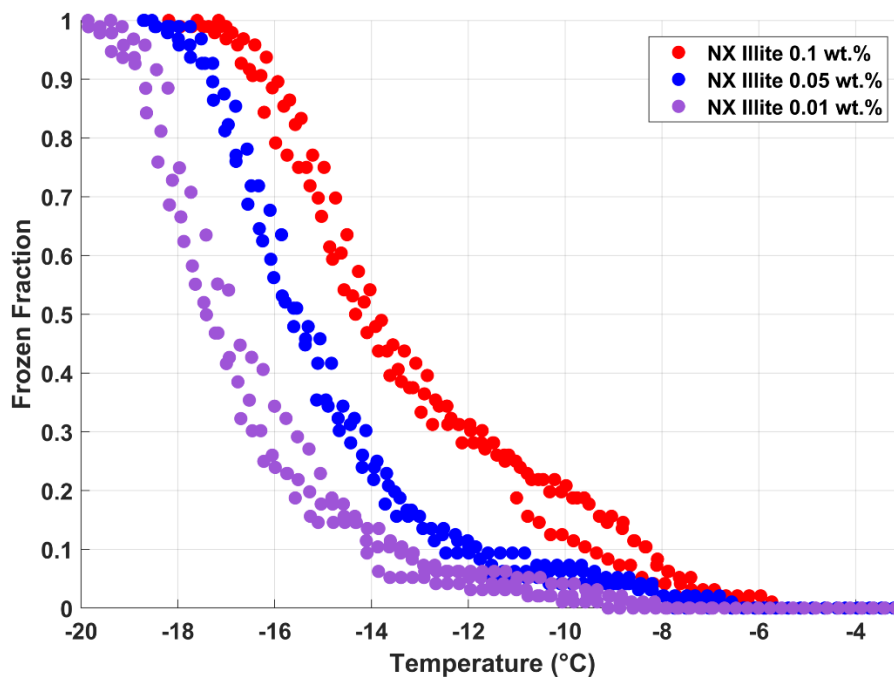


571



572

573 **Figure A3.** A side by side comparison of box plots for the freezing temperatures of the 20 SA water experiments of the reference
574 wells (left box) and the well represented by the location (right box) of each subplot. The median (red line), inter-quartile range (blue
575 box), extreme values not considered outliers (whiskers) and outliers (red crosses) are shown as a function of temperature in °C (y-
576 axes).



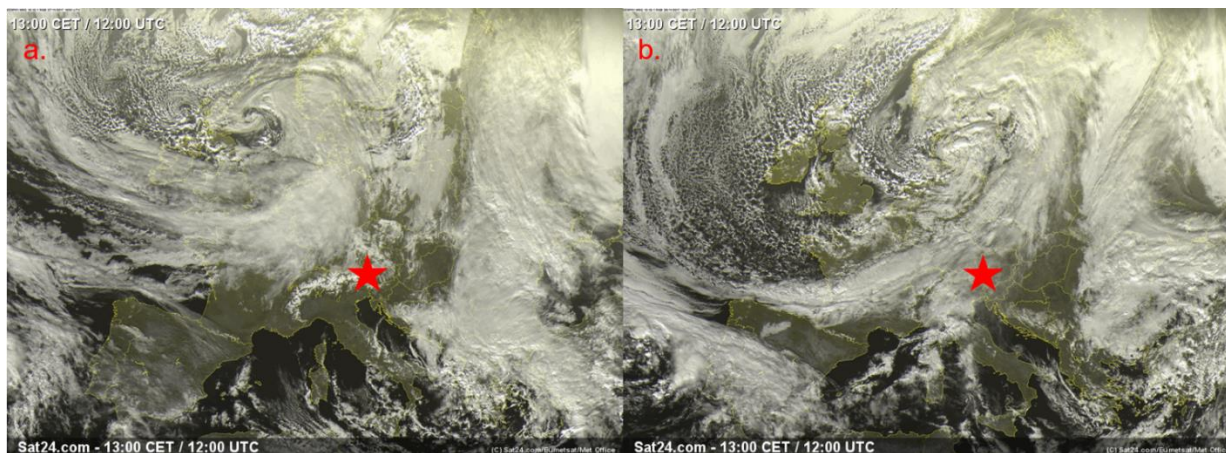
577

578

579

Figure A4. Frozen fraction curves of solutions of 0.01 wt. % (magenta dots), 0.05 wt. % (red dots) and 0.01 wt. % (purple dots) of NX-illite run in triplicates.

580

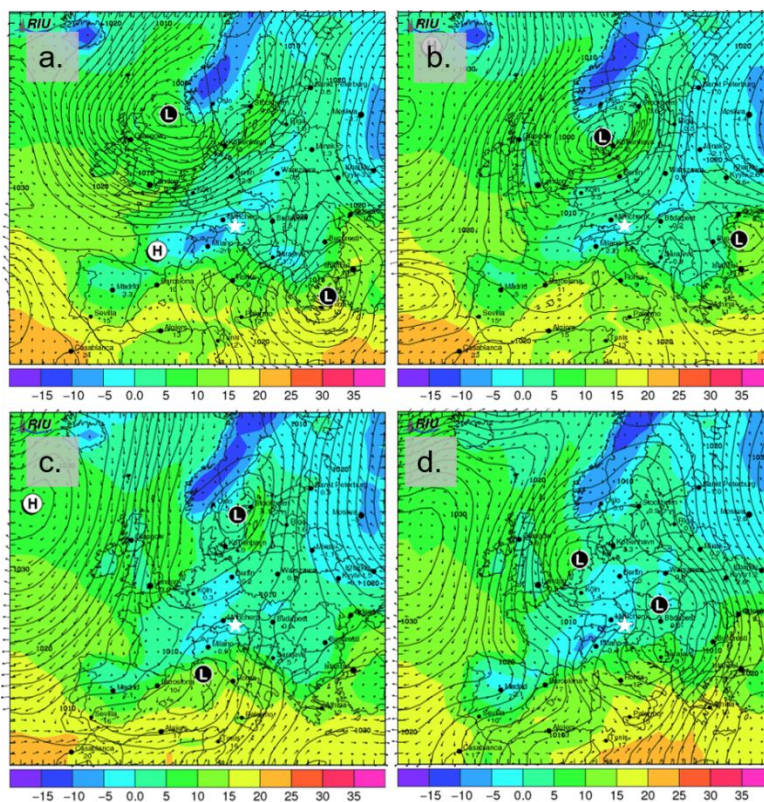


581

582

583

Figure A5: Visible satellite image of the storm system impacting the SBO (red star) taken at 1200UTC on (a) Nov. 27th and (b) 28th. Images courtesy of Sat24.com/Eumetsat/Met Office (<http://www.sat24.com/history.aspx>).

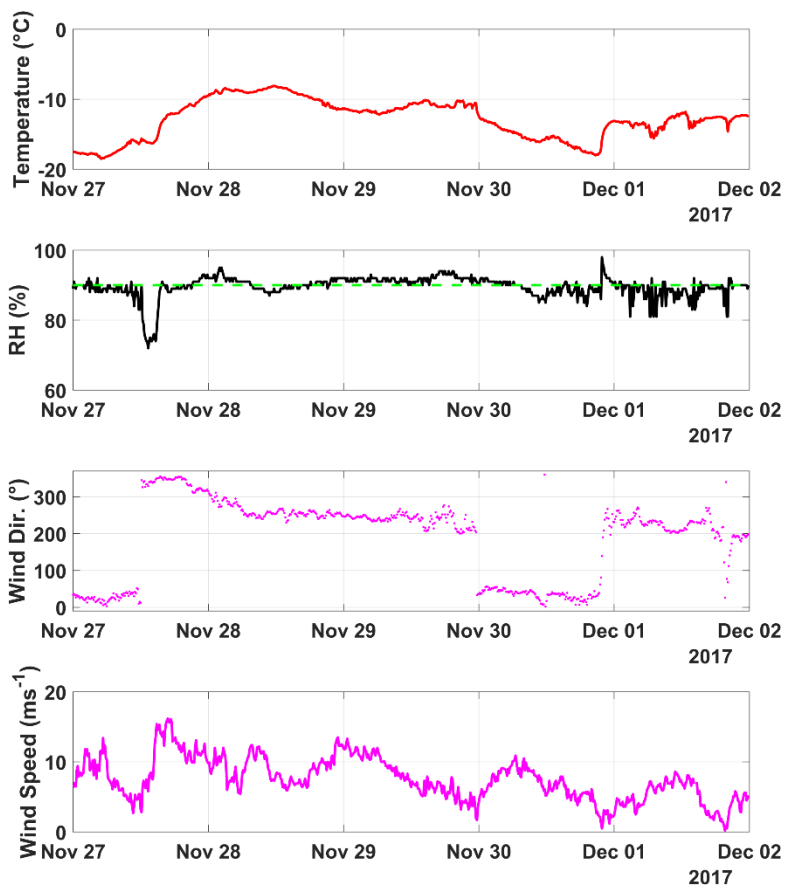


584

585 **Figure A6:** Forecasted surface pressure in hPa (black contours), 2 meter surface temperature in °C (color fill), and wind vectors in
586 m/s (black arrows) for 12 UTC on (a) 27th, (b) 28th, (c) 29th and (d) 30th. Forecasts are based on model runs initialized on 00 UTC
587 of the day of interest (12 hours before shown values). Surface low and high pressure centers are indicated with L and H, respectively.
588 The location of SBO is shown by the white star. Images are taken and adapted from the Rhenish Institute for Environmental
589 Research at the University of Cologne (http://www.uni-koeln.de/math-nat-fak/geomat/eurad/index_e.html).

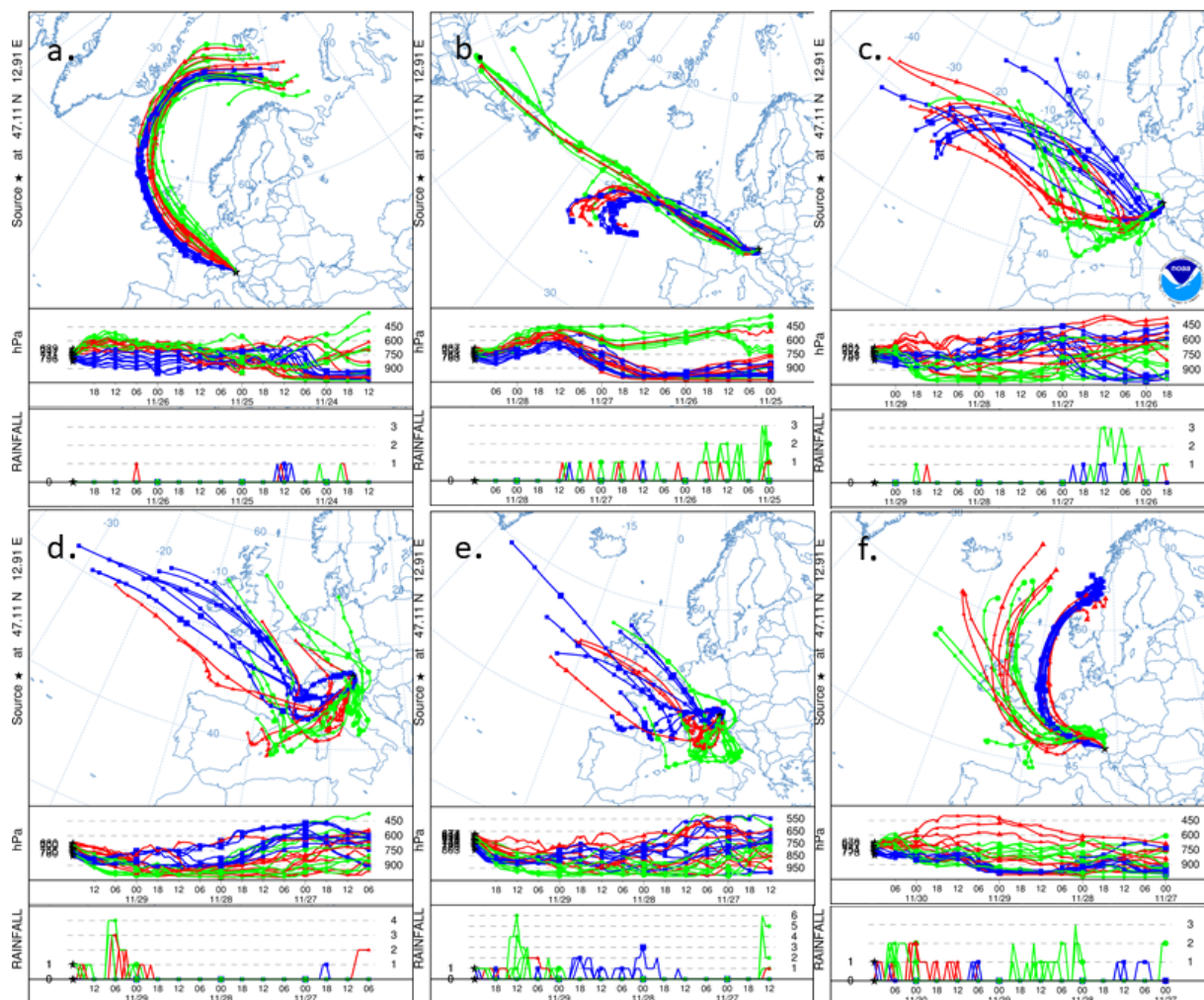


590



591

592 **Figure A7:** (top panel) Temperature ($^{\circ}\text{C}$), (top-middle panel) humidity (%), (bottom-middle panel) wind direction ($^{\circ}$) and (bottom
593 panel) wind speed (ms^{-1}) as a function of date spanning from the 27th of November to the 2nd of December (in UTC). The humidity
594 when cloud is present at SBO (90%) is shown (dashed green line).



595

596

597

598

599

600

601

602

603

604

Figure A8: (a) 84-hour HYSPLIT back trajectories from the Sonnblick Observatory initialized on 00 UTC on the 27th, (b) 12 UTC on the 28th, (c) 06 UTC and (d) 18 UTC on the 29th, and (e) 00 UTC and (f) 12 UTC on the 30th of November. The blue, green and red lines represent 8 ensemble back trajectories initialized 1000 m, 2000 m and 3000 m above the model terrain height, respectively. The two lower panels in each subplot show the back trajectory height in units of pressure (hPa) and rainfall (mm) as a function of time (in 6 hourly intervals) as a function of pressure (in hPa).



605 **References**

- 606 Ansmann, A., Tesche, M., Seifert, P., Althausen, D., Engelmann, R., Fruntke, J., Wandinger, U., Mattis, I. and Müller, D.:
607 Evolution of the ice phase in tropical altocumulus: SAMUM lidar observations over Cape Verde, *J. Geophys. Res.*
608 *Atmospheres*, 114(D17), doi:10.1029/2008JD011659, 2009.
- 609 Atherton, T. J. and Kerbyson, D. J.: *Size Invariant Circle Detection.*, 1999.
- 610 Atkinson, J. D., Murray, B. J., Woodhouse, M. T., Whale, T. F., Baustian, K. J., Carslaw, K. S., Dobbie, S., O’Sullivan, D.
611 and Malkin, T. L.: The importance of feldspar for ice nucleation by mineral dust in mixed-phase clouds, *Nature*, 498(7454),
612 355, doi:10.1038/nature12278, 2013.
- 613 Ault, A. P., Williams, C. R., White, A. B., Neiman, P. J., Creamean, J. M., Gaston, C. J., Ralph, F. M. and Prather, K. A.:
614 Detection of Asian dust in California orographic precipitation, *J. Geophys. Res. Atmospheres*, 116(D16),
615 doi:10.1029/2010JD015351, 2011.
- 616 Beall, C. M., Stokes, M. D., Hill, T. C., DeMott, P. J., DeWald, J. T. and Prather, K. A.: Automation and heat transfer
617 characterization of immersion mode spectroscopy for analysis of ice nucleating particles, *Atmos Meas Tech*, 10(7), 2613–
618 2626, doi:10.5194/amt-10-2613-2017, 2017.
- 619 Beck, A., Henneberger, J., Fugal, J. P., David, R. O., Lacher, L. and Lohmann, U.: Impact of surface and near-surface processes
620 on ice crystal concentrations measured at mountain-top research stations, *Atmospheric Chem. Phys.*, 18(12), 8909–8927,
621 doi:https://doi.org/10.5194/acp-18-8909-2018, 2018.
- 622 Bigg, E. K.: The formation of atmospheric ice crystals by the freezing of droplets, *Q. J. R. Meteorol. Soc.*, 79(342), 510–519,
623 doi:10.1002/qj.49707934207, 1953.
- 624 Boer, G. de, Morrison, H., Shupe, M. D. and Hildner, R.: Evidence of liquid dependent ice nucleation in high-latitude stratiform
625 clouds from surface remote sensors, *Geophys. Res. Lett.*, 38(1), doi:10.1029/2010GL046016, 2011.
- 626 Boose, Y., Welti, A., Atkinson, J., Ramelli, F., Danielczok, A., Bingemer, H. G., Plötze, M., Sierau, B., Kanji, Z. A. and
627 Lohmann, U.: Heterogeneous ice nucleation on dust particles sourced from nine deserts worldwide – Part 1: Immersion
628 freezing, *Atmospheric Chem. Phys.*, 16(23), 15075–15095, doi:https://doi.org/10.5194/acp-16-15075-2016, 2016a.
- 629 Boose, Y., Kanji, Z. A., Kohn, M., Sierau, B., Zipori, A., Crawford, I., Lloyd, G., Bukowiecki, N., Herrmann, E., Kupiszewski,
630 P., Steinbacher, M. and Lohmann, U.: Ice Nucleating Particle Measurements at 241 K during Winter Months at 3580 m MSL
631 in the Swiss Alps, *J. Atmospheric Sci.*, 73(5), 2203–2228, doi:10.1175/JAS-D-15-0236.1, 2016b.
- 632 Broadley, S. L., Murray, B. J., Herbert, R. J., Atkinson, J. D., Dobbie, S., Malkin, T. L., Condliffe, E. and Neve, L.: Immersion
633 mode heterogeneous ice nucleation by an illite rich powder representative of atmospheric mineral dust, *Atmos Chem Phys*,
634 12(1), 287–307, doi:10.5194/acp-12-287-2012, 2012.
- 635 Burkert-Kohn, M., Wex, H., Welti, A., Hartmann, S., Grawe, S., Hellner, L., Herenz, P., Atkinson, J. D., Stratmann, F. and
636 Kanji, Z. A.: Leipzig Ice Nucleation chamber Comparison (LINC): intercomparison of four online ice nucleation counters,
637 *Atmos Chem Phys*, 17(18), 11683–11705, doi:10.5194/acp-17-11683-2017, 2017.
- 638 Christner, B. C., Cai, R., Morris, C. E., McCarter, K. S., Foreman, C. M., Skidmore, M. L., Montross, S. N. and Sands, D. C.:
639 Geographic, seasonal, and precipitation chemistry influence on the abundance and activity of biological ice nucleators in rain
640 and snow, *Proc. Natl. Acad. Sci.*, 105(48), 18854–18859, doi:10.1073/pnas.0809816105, 2008.



- 641 Creamean, J. M., Suski, K. J., Rosenfeld, D., Cazorla, A., DeMott, P. J., Sullivan, R. C., White, A. B., Ralph, F. M., Minnis,
642 P., Comstock, J. M., Tomlinson, J. M. and Prather, K. A.: Dust and Biological Aerosols from the Sahara and Asia Influence
643 Precipitation in the Western U.S., *Science*, 339(6127), 1572–1578, doi:10.1126/science.1227279, 2013.
- 644 Cziczo, D. J., Ladino, L., Boose, Y., Kanji, Z. A., Kupiszewski, P., Lance, S., Mertes, S. and Wex, H.: Measurements of Ice
645 Nucleating Particles and Ice Residuals, *Meteorol. Monogr.*, 58, 8.1-8.13, doi:10.1175/AMSMONOGRAPHS-D-16-0008.1,
646 2017.
- 647 DeMott, P. J., Cziczo, D. J., Prenni, A. J., Murphy, D. M., Kreidenweis, S. M., Thomson, D. S., Borys, R. and Rogers, D. C.:
648 Measurements of the concentration and composition of nuclei for cirrus formation, *Proc. Natl. Acad. Sci. U. S. A.*, 100(25),
649 14655–14660, doi:10.1073/pnas.2532677100, 2003.
- 650 DeMott, P. J., Prenni, A. J., McMeeking, G. R., Sullivan, R. C., Petters, M. D., Tobo, Y., Niemand, M., Möhler, O., Snider, J.
651 R., Wang, Z. and Kreidenweis, S. M.: Integrating laboratory and field data to quantify the immersion freezing ice nucleation
652 activity of mineral dust particles, *Atmospheric Chem. Phys.*, 15(1), 393–409, doi:10.5194/acp-15-393-2015, 2015.
- 653 DeMott, P. J., Hill, T. C. J., McCluskey, C. S., Prather, K. A., Collins, D. B., Sullivan, R. C., Ruppel, M. J., Mason, R. H.,
654 Irish, V. E., Lee, T., Hwang, C. Y., Rhee, T. S., Snider, J. R., McMeeking, G. R., Dhaniyala, S., Lewis, E. R., Wentzell, J. J.
655 B., Abbatt, J., Lee, C., Sultana, C. M., Ault, A. P., Axson, J. L., Martinez, M. D., Venero, I., Santos-Figueroa, G., Stokes, M.
656 D., Deane, G. B., Mayol-Bracero, O. L., Grassian, V. H., Bertram, T. H., Bertram, A. K., Moffett, B. F. and Franc, G. D.: Sea
657 spray aerosol as a unique source of ice nucleating particles, *Proc. Natl. Acad. Sci.*, 113(21), 5797–5803,
658 doi:10.1073/pnas.1514034112, 2016.
- 659 DeMott, P. J., Hill, T. C. J., Petters, M. D., Bertram, A. K., Tobo, Y., Mason, R. H., Suski, K. J., McCluskey, C. S., Levin, E.
660 J. T., Schill, G. P., Boose, Y., Rauker, A. M., Miller, A. J., Zaragoza, J., Rocci, K., Rothfuss, N. E., Taylor, H. P., Hader, J.
661 D., Chou, C., Huffman, J. A., Pöschl, U., Prenni, A. J. and Kreidenweis, S. M.: Comparative measurements of ambient
662 atmospheric concentrations of ice nucleating particles using multiple immersion freezing methods and a continuous flow
663 diffusion chamber, *Atmospheric Chem. Phys.*, 17(18), 11227–11245, doi:10.5194/acp-17-11227-2017, 2017.
- 664 Derrick, B. and White, P.: Why Welch’s test is Type I error robust, *Quant. Methods Psychol.*, 12, 30–38,
665 doi:10.20982/tqmp.12.1.p030, 2016.
- 666 Felgitsch, L., Baloh, P., Burkart, J., Mayr, M., Momken, M. E., Seifried, T. M., Winkler, P., Schmale III, D. G. and Grothe,
667 H.: Birch leaves and branches as a source of ice-nucleating macromolecules, *Atmospheric Chem. Phys.*, 18(21), 16063–16079,
668 doi:https://doi.org/10.5194/acp-18-16063-2018, 2018.
- 669 Field, P. R., Möhler, O., Connolly, P., Krämer, M., Cotton, R., Heymsfield, A. J., Saathoff, H. and Schnaiter, M.: Some ice
670 nucleation characteristics of Asian and Saharan desert dust, *Atmos Chem Phys*, 6(10), 2991–3006, doi:10.5194/acp-6-2991-
671 2006, 2006.
- 672 Fletcher, N. H.: *The physics of rainclouds*, Cambridge University Press., 1962.
- 673 Harrison, A. D., Whale, T. F., Rutledge, R., Lamb, S., Tarn, M. D., Porter, G. C. E., Adams, M. P., McQuaid, J. B., Morris,
674 G. J. and Murray, B. J.: An instrument for quantifying heterogeneous ice nucleation in multiwell plates using infrared emissions
675 to detect freezing, *Atmospheric Meas. Tech.*, 11(10), 5629–5641, doi:https://doi.org/10.5194/amt-11-5629-2018, 2018.
- 676 Hartmann, S., Niedermeier, D., Voigtländer, J., Clauss, T., Shaw, R. A., Wex, H., Kiselev, A. and Stratmann, F.: Homogeneous
677 and heterogeneous ice nucleation at LACIS: operating principle and theoretical studies, *Atmos Chem Phys*, 11(4), 1753–
678 1767, doi:10.5194/acp-11-1753-2011, 2011.



- 679 Hill, T. C. J., Moffett, B. F., DeMott, P. J., Georgakopoulos, D. G., Stump, W. L. and Franc, G. D.: Measurement of Ice
680 Nucleation-Active Bacteria on Plants and in Precipitation by Quantitative PCR, *Appl. Environ. Microbiol.*, 80(4), 1256–1267,
681 doi:10.1128/AEM.02967-13, 2014.
- 682 Hiranuma, N., Augustin-Bauditz, S., Bingemer, H., Budke, C., Curtius, J., Danielczok, A., Diehl, K., Dreischmeier, K., Ebert,
683 M., Frank, F., Hoffmann, N., Kandler, K., Kiselev, A., Koop, T., Leisner, T., Möhler, O., Nillius, B., Peckhaus, A., Rose, D.,
684 Weinbruch, S., Wex, H., Boose, Y., DeMott, P. J., Hader, J. D., Hill, T. C. J., Kanji, Z. A., Kulkarni, G., Levin, E. J. T.,
685 McCluskey, C. S., Murakami, M., Murray, B. J., Niedermeier, D., Petters, M. D., O’Sullivan, D., Saito, A., Schill, G. P., Tajiri,
686 T., Tolbert, M. A., Welti, A., Whale, T. F., Wright, T. P. and Yamashita, K.: A comprehensive laboratory study on the
687 immersion freezing behavior of illite NX particles: a comparison of 17 ice nucleation measurement techniques, *Atmos Chem*
688 *Phys*, 15(5), 2489–2518, doi:10.5194/acp-15-2489-2015, 2015.
- 689 Hiranuma, N., Adachi, K., Bell, D. M., Belosi, F., Beydoun, H., Bhaduri, B., Bingemer, H., Budke, C., Clemen, H.-C., Conen,
690 F., Cory, K. M., Curtius, J., DeMott, P. J., Eppers, O., Grawe, S., Hartmann, S., Hoffmann, N., Höhler, K., Jantsch, E., Kiselev,
691 A., Koop, T., Kulkarni, G., Mayer, A., Murakami, M., Murray, B. J., Nicosia, A., Petters, M. D., Piazza, M., Polen, M., Reicher,
692 N., Rudich, Y., Saito, A., Santachiara, G., Schiebel, T., Schill, G. P., Schneider, J., Segev, L., Stopelli, E., Sullivan, R. C.,
693 Suski, K., Szakáll, M., Tajiri, T., Taylor, H., Tobo, Y., Ullrich, R., Weber, D., Wex, H., Whale, T. F., Whiteside, C. L.,
694 Yamashita, K., Zelenyuk, A. and Möhler, O.: A comprehensive characterization of ice nucleation by three different types of
695 cellulose particles immersed in water, *Atmospheric Chem. Phys.*, 19(7), 4823–4849, doi:https://doi.org/10.5194/acp-19-4823-
696 2019, 2019.
- 697 Hoose, C. and Möhler, O.: Heterogeneous ice nucleation on atmospheric aerosols: a review of results from laboratory
698 experiments, *Atmos Chem Phys*, 12(20), 9817–9854, doi:10.5194/acp-12-9817-2012, 2012.
- 699 Irish, V. E., Elizondo, P., Chen, J., Chou, C., Charette, J., Lizotte, M., Ladino, L. A., Wilson, T. W., Gosselin, M., Murray, B.
700 J., Polishchuk, E., Abbatt, J. P. D., Miller, L. A. and Bertram, A. K.: Ice-nucleating particles in Canadian Arctic sea-surface
701 microlayer and bulk seawater, *Atmos Chem Phys*, 17(17), 10583–10595, doi:10.5194/acp-17-10583-2017, 2017.
- 702 Kanji, Z. A., Ladino, L. A., Wex, H., Boose, Y., Burkert-Kohn, M., Cziczo, D. J. and Krämer, M.: Overview of Ice Nucleating
703 Particles, *Meteorol. Monogr.*, 58, 1.1-1.33, doi:10.1175/AMSMONOGRAPHS-D-16-0006.1, 2017.
- 704 Kaufmann, L., Marcolli, C., Hofer, J., Pinti, V., Hoyle, C. R. and Peter, T.: Ice nucleation efficiency of natural dust samples
705 in the immersion mode, *Atmospheric Chem. Phys.*, 16(17), 11177–11206, doi:https://doi.org/10.5194/acp-16-11177-2016,
706 2016.
- 707 Kaufmann, L., Marcolli, C., Luo, B. and Peter, T.: Refreeze experiments with water droplets containing different types of ice
708 nuclei interpreted by classical nucleation theory, *Atmos Chem Phys*, 17(5), 3525–3552, doi:10.5194/acp-17-3525-2017, 2017.
- 709 Kohn, M., Lohmann, U., Welti, A. and Kanji, Z. A.: Immersion mode ice nucleation measurements with the new Portable
710 Immersion Mode Cooling chamber (PIMCA), *J. Geophys. Res. Atmospheres*, 121(9), 4713–4733,
711 doi:10.1002/2016JD024761, 2016.
- 712 Lacher, L., Lohmann, U., Boose, Y., Zipori, A., Herrmann, E., Bukowiecki, N., Steinbacher, M. and Kanji, Z. A.: The
713 Horizontal Ice Nucleation Chamber (HINC): INP measurements at conditions relevant for mixed-phase clouds at the High
714 Altitude Research Station Jungfraujoch, *Atmospheric Chem. Phys.*, 17(24), 15199–15224, doi:https://doi.org/10.5194/acp-17-
715 15199-2017, 2017.
- 716 Lacher, L., Steinbacher, M., Bukowiecki, N., Herrmann, E., Zipori, A. and Kanji, Z. A.: Impact of Air Mass Conditions and
717 Aerosol Properties on Ice Nucleating Particle Concentrations at the High Altitude Research Station Jungfraujoch, *Atmosphere*,
718 9(9), 363, doi:10.3390/atmos9090363, 2018.



- 719 Lohmann, U. and Feichter, J.: Global indirect aerosol effects: a review, *Atmos Chem Phys*, 5(3), 715–737, doi:10.5194/acp-
720 5-715-2005, 2005.
- 721 Lowenthal, D., Hallar, A. G., McCubbin, I., David, R., Borys, R., Blossey, P., Muhlbauer, A., Kuang, Z. and Moore, M.:
722 Isotopic Fractionation in Wintertime Orographic Clouds, *J. Atmospheric Ocean. Technol.*, 33(12), 2663–2678,
723 doi:10.1175/JTECH-D-15-0233.1, 2016.
- 724 Lüönd, F., Stetzer, O., Welti, A. and Lohmann, U.: Experimental study on the ice nucleation ability of size-selected kaolinite
725 particles in the immersion mode, *J. Geophys. Res. Atmospheres*, 115(D14), doi:10.1029/2009JD012959, 2010.
- 726 Marcolli, C., Gedamke, S., Peter, T. and Zobrist, B.: Efficiency of immersion mode ice nucleation on surrogates of mineral
727 dust, *Atmos Chem Phys*, 7(19), 5081–5091, doi:10.5194/acp-7-5081-2007, 2007.
- 728 Matus, A. V. and L’Ecuyer, T. S.: The role of cloud phase in Earth’s radiation budget, *J. Geophys. Res. Atmospheres*, 122(5),
729 2559–2578, doi:10.1002/2016JD025951, 2017.
- 730 McCluskey, C. S., Ovadnevaite, J., Rinaldi, M., Atkinson, J., Belosi, F., Ceburnis, D., Marullo, S., Hill, T. C. J., Lohmann, U.,
731 Kanji, Z. A., O’Dowd, C., Kreidenweis, S. M. and DeMott, P. J.: Marine and Terrestrial Organic Ice-Nucleating Particles in
732 Pristine Marine to Continentally Influenced Northeast Atlantic Air Masses, *J. Geophys. Res. Atmospheres*, 123(11), 6196–
733 6212, doi:10.1029/2017JD028033, 2018.
- 734 Mühlstenstädt, J., Sourdeval, O., Delanoë, J. and Quaas, J.: Frequency of occurrence of rain from liquid-, mixed-, and ice-phase
735 clouds derived from A-Train satellite retrievals: RAIN FROM LIQUID- AND ICE-PHASE CLOUDS, *Geophys. Res. Lett.*,
736 42(15), 6502–6509, doi:10.1002/2015GL064604, 2015.
- 737 Murray, B. J., L. Broadley, S., W. Wilson, T., J. Bull, S., H. Wills, R., K. Christenson, H. and J. Murray, E.: Kinetics of the
738 homogeneous freezing of water, *Phys. Chem. Chem. Phys.*, 12(35), 10380–10387, doi:10.1039/C003297B, 2010.
- 739 Murray, B. J., O’Sullivan, D., D. Atkinson, J. and E. Webb, M.: Ice nucleation by particles immersed in supercooled cloud
740 droplets, *Chem. Soc. Rev.*, 41(19), 6519–6554, doi:10.1039/C2CS35200A, 2012.
- 741 Niemand, M., Möhler, O., Vogel, B., Vogel, H., Hoose, C., Connolly, P., Klein, H., Bingemer, H., DeMott, P., Skrotzki, J. and
742 Leisner, T.: A Particle-Surface-Area-Based Parameterization of Immersion Freezing on Desert Dust Particles, *J. Atmospheric
743 Sci.*, 69(10), 3077–3092, doi:10.1175/JAS-D-11-0249.1, 2012.
- 744 Petters, M. D. and Wright, T. P.: Revisiting ice nucleation from precipitation samples, *Geophys. Res. Lett.*, 42(20), 8758–
745 8766, doi:10.1002/2015GL065733, 2015.
- 746 Polen, M., Brubaker, T., Somers, J. and Sullivan, R. C.: Cleaning up our water: reducing interferences from non-homogeneous
747 freezing of H_2O water in droplet freezing assays of ice nucleating particles, *Atmospheric Meas. Tech. Discuss.*, 1–31,
748 doi:https://doi.org/10.5194/amt-2018-134, 2018.
- 749 Pummer, B. G., Bauer, H., Bernardi, J., Bleicher, S. and Grothe, H.: Suspendable macromolecules are responsible for ice
750 nucleation activity of birch and conifer pollen, *Atmos Chem Phys*, 12(5), 2541–2550, doi:10.5194/acp-12-2541-2012, 2012.
- 751 Puxbaum, H. and Tschewenka, W.: Relationships of major ions in snow fall and rime at sonnblick observatory (SBO, 3106m)
752 and implications for scavenging processes in mixed clouds, *Atmos. Environ.*, 32(23), 4011–4020, doi:10.1016/S1352-
753 2310(98)00244-1, 1998.



- 754 Reicher, N., Segev, L. and Rudich, Y.: The Weizmann Supercooled Droplets Observation on a Microarray (WISDOM) and
755 application for ambient dust, *Atmos Meas Tech*, 11(1), 233–248, doi:10.5194/amt-11-233-2018, 2018.
- 756 Richardson, M. S., DeMott, P. J., Kreidenweis, S. M., Cziczo, D. J., Dunlea, E. J., Jimenez, J. L., Thomson, D. S., Ashbaugh,
757 L. L., Borys, R. D., Westphal, D. L., Casuccio, G. S. and Lersch, T. L.: Measurements of heterogeneous ice nuclei in the
758 western United States in springtime and their relation to aerosol characteristics, *J. Geophys. Res. Atmospheres*, 112(D2),
759 D02209, doi:10.1029/2006JD007500, 2007.
- 760 Riechers, B., Wittbracht, F., H?tten, A. and Koop, T.: The homogeneous ice nucleation rate of water droplets produced in a
761 microfluidic device and the role of temperature uncertainty, *Phys. Chem. Chem. Phys.*, 15(16), 5873, doi:10.1039/c3cp42437e,
762 2013.
- 763 Roebber, P. J., Bruening, S. L., Schultz, D. M. and Cortinas, J. V.: Improving Snowfall Forecasting by Diagnosing Snow
764 Density, *Weather Forecast.*, 18(2), 264–287, doi:10.1175/1520-0434(2003)018<0264:ISFBDS>2.0.CO;2, 2003.
- 765 Rogers, D. C.: Development of a continuous flow thermal gradient diffusion chamber for ice nucleation studies, *Atmospheric*
766 *Res.*, 22(2), 149–181, doi:10.1016/0169-8095(88)90005-1, 1988.
- 767 Rolph, G., Stein, A. and Stunder, B.: Real-time Environmental Applications and Display sYstem: READY, *Environ. Model.*
768 *Softw.*, 95, 210–228, doi:10.1016/j.envsoft.2017.06.025, 2017.
- 769 Spiess, A.-N., Feig, C. and Ritz, C.: Highly accurate sigmoidal fitting of real-time PCR data by introducing a parameter for
770 asymmetry, *BMC Bioinformatics*, 9, 221, doi:10.1186/1471-2105-9-221, 2008.
- 771 Stan, C. A., Schneider, G. F., Shevkopyas, S. S., Hashimoto, M., Ibanescu, M., Wiley, B. J. and Whitesides, G. M.: A
772 microfluidic apparatus for the study of ice nucleation in supercooled water drops, *Lab. Chip*, 9(16), 2293–2305,
773 doi:10.1039/B906198C, 2009.
- 774 Stein, A. F., Draxler, R. R., Rolph, G. D., Stunder, B. J. B., Cohen, M. D. and Ngan, F.: NOAA’s HYSPLIT Atmospheric
775 Transport and Dispersion Modeling System, *Bull. Am. Meteorol. Soc.*, 96(12), 2059–2077, doi:10.1175/BAMS-D-14-
776 00110.1, 2015.
- 777 Stetzer, O., Baschek, B., Lüönd, F. and Lohmann, U.: The Zurich Ice Nucleation Chamber (ZINC)-A New Instrument to
778 Investigate Atmospheric Ice Formation, *Aerosol Sci. Technol.*, 42(1), 64–74, doi:10.1080/02786820701787944, 2008.
- 779 Stopelli, E., Conen, F., Zimmermann, L., Alewell, C. and Morris, C. E.: Freezing nucleation apparatus puts new slant on study
780 of biological ice nucleators in precipitation, *Atmospheric Meas. Tech.*, 7(1), 129–134, doi:10.5194/amt-7-129-2014, 2014.
- 781 Stopelli, E., Conen, F., Morris, C. E., Herrmann, E., Bukowiecki, N. and Alewell, C.: Ice nucleation active particles are
782 efficiently removed by precipitating clouds, *Sci. Rep.*, 5, 16433, doi:10.1038/srep16433, 2015.
- 783 Tan, I., Storelvmo, T. and Zelinka, M. D.: Observational constraints on mixed-phase clouds imply higher climate sensitivity,
784 *Science*, 352(6282), 224–227, doi:10.1126/science.aad5300, 2016.
- 785 Tarn, M. D., Sikora, S. N. F., Porter, G. C. E., O’Sullivan, D., Adams, M., Whale, T. F., Harrison, A. D., Vergara-Temprado,
786 J., Wilson, T. W., Shim, J. and Murray, B. J.: The study of atmospheric ice-nucleating particles via microfluidically generated
787 droplets, *Microfluid. Nanofluidics*, 22(5), doi:10.1007/s10404-018-2069-x, 2018.
- 788 Vali, G.: Quantitative Evaluation of Experimental Results an the Heterogeneous Freezing Nucleation of Supercooled Liquids,
789 *J. Atmospheric Sci.*, 28(3), 402–409, doi:10.1175/1520-0469(1971)028<0402:QEOERA>2.0.CO;2, 1971.



- 790 Vali, G.: Revisiting the differential freezing nucleus spectra derived from drop-freezing experiments: methods of calculation,
791 applications, and confidence limits, *Atmospheric Meas. Tech.*, 12(2), 1219–1231, doi:https://doi.org/10.5194/amt-12-1219-
792 2019, 2019.
- 793 Vali, G., DeMott, P. J., Möhler, O. and Whale, T. F.: Technical Note: A proposal for ice nucleation terminology, *Atmospheric*
794 *Chem. Phys.*, 15(18), 10263–10270, doi:10.5194/acp-15-10263-2015, 2015.
- 795 Welti, A., Müller, K., Fleming, Z. L. and Stratmann, F.: Concentration and variability of ice nuclei in the subtropical maritime
796 boundary layer, *Atmos Chem Phys*, 18(8), 5307–5320, doi:10.5194/acp-18-5307-2018, 2018.
- 797 Westbrook, C. D. and Illingworth, A. J.: Evidence that ice forms primarily in supercooled liquid clouds at temperatures >
798 -27°C , *Geophys. Res. Lett.*, 38(14), doi:10.1029/2011GL048021, 2011.
- 799 Wex, H., Augustin-Bauditz, S., Boose, Y., Budke, C., Curtius, J., Diehl, K., Dreyer, A., Frank, F., Hartmann, S., Hiranuma,
800 N., Jantsch, E., Kanji, Z. A., Kiselev, A., Koop, T., Möhler, O., Niedermeier, D., Nillius, B., Rösch, M., Rose, D., Schmidt,
801 C., Steinke, I. and Stratmann, F.: Intercomparing different devices for the investigation of ice nucleating particles using
802 Snomax[®] as test substance, *Atmospheric Chem. Phys.*, 15(3), 1463–1485, doi:10.5194/acp-15-1463-
803 2015, 2015.
- 804 Wex, H., Huang, L., Zhang, W., Hung, H., Traversi, R., Becagli, S., Sheesley, R. J., Moffett, C. E., Barrett, T. E., Bossi, R.,
805 Skov, H., Hünerbein, A., Lubitz, J., Löffler, M., Linke, O., Hartmann, M., Herenz, P. and Stratmann, F.: Annual variability of
806 ice-nucleating particle concentrations at different Arctic locations, *Atmospheric Chem. Phys.*, 19(7), 5293–5311,
807 doi:https://doi.org/10.5194/acp-19-5293-2019, 2019.
- 808 Whale, T. F., Murray, B. J., O’Sullivan, D., Wilson, T. W., Umo, N. S., Baustian, K. J., Atkinson, J. D., Workneh,
809 D. A. and Morris, G. J.: A technique for quantifying heterogeneous ice nucleation in microlitre supercooled water droplets,
810 *Atmospheric Meas. Tech.*, 8(6), 2437–2447, doi:10.5194/amt-8-2437-2015, 2015.
- 811 Wilson, T. W., Ladino, L. A., Alpert, P. A., Breckels, M. N., Brooks, I. M., Browse, J., Burrows, S. M., Carslaw, K. S.,
812 Huffman, J. A., Judd, C., Kilhau, W. P., Mason, R. H., McFiggans, G., Miller, L. A., Nájera, J. J., Polishchuk, E., Rae, S.,
813 Schiller, C. L., Si, M., Temprado, J. V., Whale, T. F., Wong, J. P. S., Wurl, O., Yakobi-Hancock, J. D., Abbatt, J. P. D., Aller,
814 J. Y., Bertram, A. K., Knopf, D. A. and Murray, B. J.: A marine biogenic source of atmospheric ice-nucleating particles,
815 *Nature*, 525(7568), 234, doi:10.1038/nature14986, 2015.

816